NRLMSIS 2.0: A Whole-Atmosphere Empirical Model of Temperature and Neutral Species Densities

J. T. Emmert[1] [ID], D. P. Drob[1] [ID], J. M. Picone[2] [ID], D. E. Siskind[1] [ID], M. Jones Jr.[1] [ID],
M. G. Mlynczak[3] [ID], P. F. Bernath[4,5] [ID], X. Chu[6,7] [ID], E. Doornbos[8], B. Funke[9] [ID],
L. P. Goncharenko[10] [ID], M. E. Hervig[11] [ID], M. J. Schwartz[12] [ID], P. E. Sheese[13] [ID], F. Vargas[14] [ID],
B. P. Williams[15] [ID], and T. Yuan[16] [ID]

[1]Space Science Division, U.S. Naval Research Laboratory, Washington, DC, USA, [2]Voluntary Emeritus Program, U.S. Naval Research Laboratory, Washington, DC, USA, [3]Science Directorate, NASA Langley Research Center, Hampton, VA, USA, [4]Department of Chemistry and Biochemistry, Old Dominion University, Norfolk, VA, USA, [5]Department of Chemistry, University of Waterloo, Waterloo, Ontario, Canada, [6]Cooperative Institute of Research in Environmental Sciences, University of Colorado Boulder, Boulder, CO, USA, [7]Department of Aerospace Engineering Sciences, University of Colorado Boulder, Boulder, CO, USA, [8]Royal Netherlands Meteorological Institute (KNMI), De Bilt, The Netherlands, [9]Instituto de Astrofísica de Andalucía, CSIC, Granada, Spain, [10]Haystack Observatory, Massachusetts Institute of Technology, Westford, MA, USA, [11]GATS, Driggs, ID, USA, [12]Jet Propulsion Laboratory, California Institute of Technology, Pasadena, CA, USA, [13]Department of Physics, University of Toronto, Toronto, Ontario, Canada, [14]Department of Electrical and Computer Engineering, University of Illinois at Urbana-Champaign, Urbana, IL, USA, [15]GATS, Boulder Division, Boulder, CO, USA, [16]Center for Atmospheric and Space Science, Utah State University, Logan, UT, USA

Abstract NRLMSIS® 2.0 is an empirical atmospheric model that extends from the ground to the exobase and describes the average observed behavior of temperature, eight species densities, and mass density via a parametric analytic formulation. The model inputs are location, day of year, time of day, solar activity, and geomagnetic activity. NRLMSIS 2.0 is a major, reformulated upgrade of the previous version, NRLMSISE-00. The model now couples thermospheric species densities to the entire column, via an effective mass profile that transitions each species from the fully mixed region below ~70 km altitude to the diffusively separated region above ~200 km. Other changes include the extension of atomic oxygen down to 50 km and the use of geopotential height as the internal vertical coordinate. We assimilated extensive new lower and middle atmosphere temperature, O, and H data, along with global average thermospheric mass density derived from satellite orbits, and we validated the model against independent samples of these data. In the mesosphere and below, residual biases and standard deviations are considerably lower than NRLMSISE-00. The new model is warmer in the upper troposphere and cooler in the stratosphere and mesosphere. In the thermosphere, N_2 and O densities are lower in NRLMSIS 2.0; otherwise, the NRLMSISE-00 thermosphere is largely retained. Future advances in thermospheric specification will likely require new in situ mass spectrometer measurements, new techniques for species density measurement between 100 and 200 km, and the reconciliation of systematic biases among thermospheric temperature and composition data sets, including biases attributable to long-term changes.

1. Introduction

An empirical atmospheric model provides a description of the average spatiotemporal behavior of atmospheric state variable observations via a parameterized analytical formulation, often with physical constraints (e.g., Emmert, 2015b). Input arguments to empirical atmospheric models typically include geographic location, day of year, time of day, and external drivers such as solar and geomagnetic activity (e.g., Bruinsma, 2015; Drob et al., 2015; Hedin, 1987; Oberheide et al., 2011). Empirical models play several indispensable roles in atmospheric research, data analysis, specification, and prediction, particularly in upper atmospheric applications. They provide a condensed representation of the historical record of observations and thereby serve as benchmarks for testing new observations and techniques. They are extensively used as a background reference for retrieving atmospheric state variables from raw measurements such as

radiances. They also often provide initial and boundary conditions for first principles models. Most directly, they are used to specify and forecast the atmosphere, particularly when contemporary or real-time data are sparse or nonexistent.

The Mass Spectrometer Incoherent Scatter radar or MSIS® series of empirical models describes atmospheric temperature, number densities of eight species, and mass density. The acronym derives from the space-based mass spectrometer and ground-based incoherent scatter radar (ISR) measurements on which the model was originally based. First developed at NASA's Goddard Space Flight Center, the model began as a thermospheric model and was eventually extended down to the ground (Hedin, 1987, 1991; Hedin, Reber, et al., 1977; Hedin, Salah, et al., 1977). In the late 1990s, development continued at the Naval Research Laboratory and resulted in NRLMSISE-00 (Picone et al., 2002). That release was focused primarily on the thermosphere and included the assimilation of new middle thermosphere O_2 data, more recent ISR measurements, mass density data derived from satellite orbit decay, and the introduction of an anomalous oxygen component that accounts for additional mass in the upper thermosphere attributed to a hot population of atomic oxygen and atomic oxygen ions.

An inherent limitation of NRLMSISE-00 was the lack of satellite data to define the composition and structure of the atmosphere below 100 km. Motivated by this deficiency, NRLMSIS 2.0 assimilates extensive new (since 2000) measurements and analyses of temperature in the mesosphere, stratosphere, and troposphere, as well as many years of new atomic oxygen (O) and atomic hydrogen (H) measurements in the mesosphere. We also tuned the model's upper thermosphere to better match new orbit-derived mass density measurements. Major changes to the model formulation have been implemented, including a temperature-dependent connection between densities in the lower/middle atmosphere and the thermosphere; in NRLMSISE-00 and earlier versions, thermospheric densities were treated independently from the lower layers, with a posteriori joining of the upper and lower profiles. NRLMSIS 2.0 densities are fully coupled to temperature from the ground to the exosphere via a hydrostatic/diffusive equilibrium profile. In this sense it can be regarded as a whole-atmosphere empirical model.

In conjunction with the mathematical reformulation, the source code was rewritten in Fortran 90 with modern programming practices. The code is available in the supporting information of this paper and in the repository listed in the acknowledgments. Version numbers will now be decimal based instead of year based. Besides producing a new reference model for the whole atmosphere, this study is also implicitly a scientific analysis of the extant modern atmospheric database, especially below the thermosphere. Because the model synthesizes the database and normalizes out the systematic agreement among data, the subsequent comparison to the individual data sets reveals systematic disagreements among the data sets. Such analysis is a major component of this study.

The new model formulation is presented in section 2. Section 3 describes the data sets used to tune and validate the model and the random sampling procedure. Section 4 describes the fitting procedure to estimate the model parameters, and section 5 summarizes statistical comparisons of the model to independent random samples of the data. In section 6, we examine mutual biases among the model and data sets and discuss scientific issues that the model and its development have illuminated. Conclusions and future development plans are summarized in section 7. Herein, NRLMSISE-00 and NRLMSIS 2.0 are often shortened to "MSISE-00" and "MSIS 2.0" for brevity; "MSIS" collectively refers to all versions of the model.

2. Model Formulation

This section summarizes the mathematical formulation of MSIS 2.0, highlighting important changes from MSISE-00. We focus on the vertical temperature and density parameterizations. Additional details of the other formulation changes are provided in the appendix and supporting information. In the new formulation, we aimed for three characteristics: a connected and continuous representation of the model components (temperature and species number densities) from ground to space, a robust closed-form solution to the species-by-species hydrostatic integral coupling temperature to species density, and sufficient flexibility to accommodate variations evident in the data, as described below.

2.1. Geopotential Height

MSIS 2.0 internally uses geopotential height (ζ) as the vertical coordinate, which simplifies the hydrostatic integral term in the density profiles (section 2.3) while fully accounting for height- and latitude-dependent gravity. All reference heights and spline nodes are defined in terms of geopotential height. In contrast, earlier versions specify reference heights and nodes on geodetic altitude levels and compute geopotential changes within each geometric shell. This change will be transparent to most users, because the input argument to the model code is geodetic altitude by default. However, the code includes an option to input geopotential height directly, which may facilitate comparison with first-principles models and data sets that are given on a geopotential grid.

We calculate geopotential height as function of geodetic altitude and latitude, relative to the World Geodetic System 1984 (WGS-84) reference ellipsoid (National Imagery and Mapping Agency, 2000) and associated gravitational field, which excludes longitudinal variations and zonal harmonics higher than order 2. The details of the calculation are provided in the appendix. A key parameter is the reference gravity, which scales the geopotential to a length; its value is somewhat arbitrary but must be applied consistently. We use the standard gravity value of 9.80665 m/s^2, which is the standard for meteorological observations (WMO, 2014, Part I, Chapter 12).

2.2. Vertical Temperature Profile

The local temperature profile is parameterized as a linear combination of cubic B-splines (de Boor, 2001) below 122.5 km and a Bates thermospheric temperature profile (Bates, 1959) above 122.5 km:

$$\frac{1}{T(\zeta)} = \begin{cases} \{T_{ex} - (T_{ex} - T_B)\exp[-\sigma(\zeta - \zeta_B)]\}^{-1} & ; \ \zeta \geq \zeta_B \\ \sum_{i=0}^{N_S - 1} \alpha_i S_i(\zeta) & ; \ \zeta < \zeta_B \end{cases}$$

$T(\zeta)$	Temperature profile as a function of geopotential height
$\zeta_B = 122.5$ km	Bates profile reference height and joining height
T_{ex}	Exospheric temperature (fitting parameter)
$T_B = T(\zeta_B)$	Temperature at ζ_B (fitting parameter)
$\sigma = T'_B/(T_{ex} - T_B)$	Shape parameter
$T'_B = \dfrac{dT}{d\zeta}\bigg|_{\zeta = \zeta_B}$	Temperature gradient at ζ_B (fitting parameter)
$N_S = 24$	Number of B-spline basis functions
α_i	Coefficients on B-spline basis functions (fitting parameters)
S_i	Cubic B-splines with nodes at heights $\zeta_{S,i}$; $i = 0$ to $N_S + 3$

(1)

$$\zeta_{S,i} = \{-15, -10, -5, 0, 5, ..., 80, 85, 92.5, 102.5, 112.5, 122.5, 132.5, 142.5, 152.5\} \text{ km}$$

The node spacing of the B-splines is 5 km below a height of 85 km, increasing to 10 km above 102.5 km. At the joining altitude $\zeta_B = 122.5$ km, the profile is constrained to be C2 continuous (continuous in the zeroth, first, and second derivatives), so that the three Bates parameters (T_{ex}, T_B, σ) determine the last three B-spline coefficients (and thereby influence the temperature down to 92.5 km). The profile is defined by 24 parameters: the first 21 B-spline coefficients and the 3 Bates parameters. Figure 1 illustrates the global average temperature profile in MSIS 2.0 and the constituent B-splines. Unless otherwise specified, "global average" herein means including only the lead term of the expansion described in section 2.4, that is, annual average, moderate solar activity ($F_{10.7} = 150$) and quiet geomagnetic activity ($Ap = 4$).

MSISE-00 also uses cubic splines and the Bates profile to represent temperature. However, there are several important differences in their application. First, MSIS 2.0 uses B-splines, whereas MSISE-00 uses spline
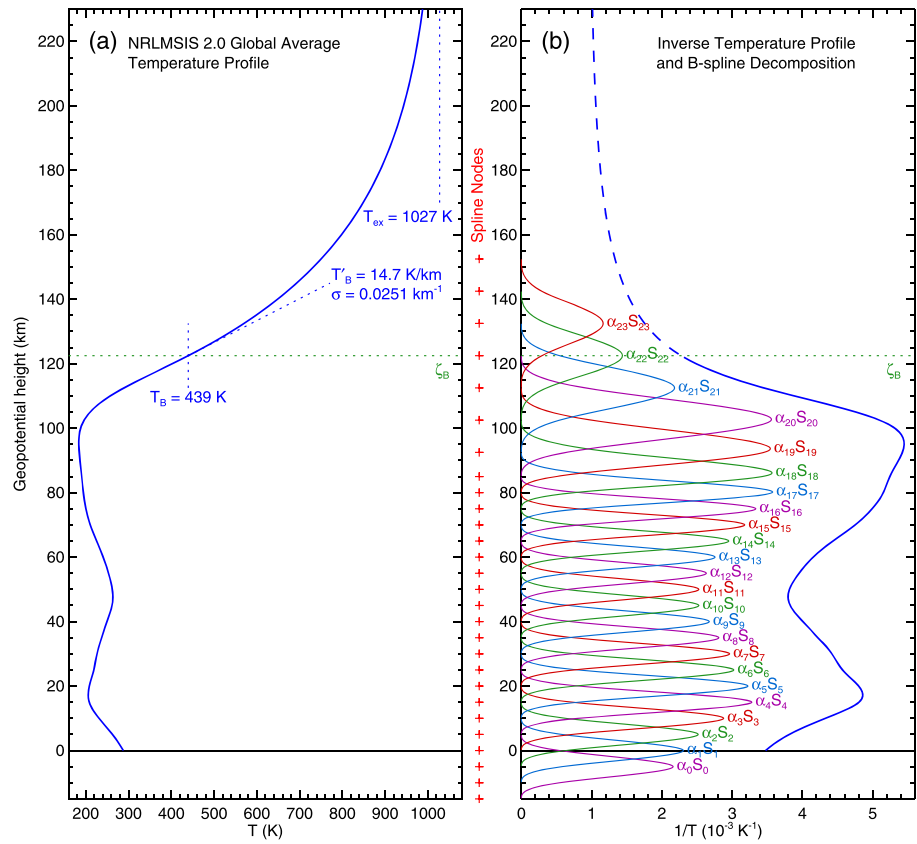
Figure 1. (a) Global average temperature profile in NRLMSIS 2.0, as a function of geopotential height. The thermospheric Bates profile parameter values are annotated. The joining height ζ_B with the spline portion of the profile is indicated by the horizontal dotted line. (b) Decomposition of the inverse of the lower part of the temperature profile in terms of the constituent B-splines. The weighted B-splines are shown (see Equation 1), annotated with their respective index numbers, along their sum, which is the inverse temperature profile (thick blue solid curve). Also shown are the inverse of the Bates portion of the profile (dashed blue line) and the locations of the B-spline nodes (red crosses).

interpolation among specified temperatures at each node. The use of B-splines renders MSIS 2.0 linear with respect to the model parameters in the spline region, which facilitates fast and robust least squares fits to data (see section 4). Second, MSIS 2.0 is C2 continuous (continuous through the second derivative) throughout the entire model domain, whereas MSISE-00 segments the atmosphere into four regions with C1 continuity (continuous through the first derivative) across the boundaries (32.5, 72.5, and 120 km). Third, the shape of the Bates profile and the meaning of the Bates temperature gradient parameter are slightly different in MSIS 2.0, due to its use of a global geopotential height coordinate rather than the geopotential height difference referenced to 120 km (Hedin, 1987, Equation A4a). Finally, MSIS 2.0 adds additional nodes to the parameterization, which provides increased vertical resolution: There are 24 vertical temperature parameters in MSIS 2.0, compared with 17 in MSISE-00. The increased resolution is supported by the new data sets described in section 3.

2.3. Vertical Density Profiles

The basic local number density profile is parameterized assuming hydrostatic balance in the lower and middle atmosphere and species-by-species hydrostatic equilibrium (which is similar to diffusive equilibrium; Picone et al., 2016) in the upper thermosphere, using an effective mass profile to transition smoothly between the two regimes. Chemical and dynamical correction terms are also applied to some species. The formulas presented in this section describe the profile of any single species; for simplicity, species subscripts are omitted.

$$\ln n(\zeta) = \ln n_0 - \frac{g_0}{k}\int_{\zeta_0}^{\zeta}\frac{M(\zeta')}{T(\zeta')}d\zeta' - \ln\frac{T(\zeta)}{T(\zeta_0)} - Ce^{-(\zeta-\zeta_c)/H_C} + R\left[1 + \tanh\left(\frac{\zeta-\zeta_R}{\gamma(\zeta)H_R}\right)\right]$$

$n(\zeta)$	Number density of a particular species
$n_0 = n(\zeta_0)$	Reference density (defined below)
ζ_0	Reference geopotential height
g_0	Reference gravitational acceleration (see equation (A3))
k	Boltzmann constant
$M(\zeta)$	Effective mass profile (defined below)
C, ζ_C, H_C	Chemical loss term parameters
R, ζ_R, H_R	Chemical/dynamical correction parameters

(2)

$$\gamma(\zeta) = \frac{1}{2}\left\{1 + \tanh\left(\frac{\zeta-\zeta_\gamma}{H_\gamma}\right)\right\}$$

$\zeta_\gamma = 70$ km

$H_\gamma = 40$ km

The first term n_0 on the right-hand side of Equation 2 scales the entire profile and (in the absence of chemical and dynamical corrections) is equal to the species density at the fiducial height ζ_0. The second term is the hydrostatic integral, which includes an effective mass profile that is described below. The third term represents the ideal gas law; this term and the hydrostatic integral couple the temperature profile to the density profile (cf. Emmert, 2015b; section 3.1). The fourth term is a Chapman-like bottomside chemical loss term (Chapman, 1931, Equation 40); the model applies this term to O, H, and N, which experience photochemical production and loss similar to that of the ionosphere. The last term is a logistic function (expressed in hyperbolic tangent form) used for chemical and/or dynamical perturbations. As described in section 4, we also use the logistic correction term to relax upper thermospheric MSIS 2.0 densities to MSISE-00. Each of the two correction terms is defined by three parameters: an amplitude (C or R), a reference height (ζ_C or ζ_R), and a scale height (H_C or H_R). While the chemical loss term has an upper asymptote of zero and is unbounded on the lower end, the chemical/dynamical correction term has a lower asymptote of zero and an upper asymptote of R. For the chemical/dynamical correction, we additionally accelerate the relaxation to the lower asymptote by applying another hyperbolic tangent taper $\gamma(\zeta)$ to H_R; this prevents the correction from projecting downward into the lower atmosphere.

To provide a monotonic transition from a single fluid state to a multifluid diffusively separated state (Picone et al., 2016), we define an effective mass profile consisting of a six-segment piecewise-linear function drawn through an asymmetric hyperbolic tangent function. The function is defined by five parameters:

$\overline{M} = 28.96546$ amu	Mass in fully mixed region (lower asymptote)
M_s	Species mass (upper asymptote)
ζ_M	Transition, or "turbopause" height
H_{ML}	Scale height of lower portion
H_{MU}	Scale height of upper portion

(3)

The asymptotes are fixed; the other three parameters may vary from species to species and according to geophysical conditions. From these five parameters, the nodes of the piecewise profile are computed as follows:
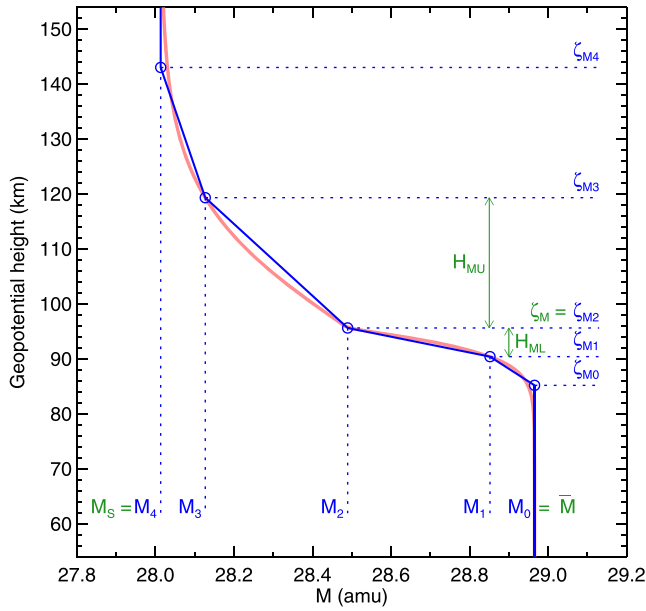
Figure 2. Global average effective mass profile for N_2 in NRLMSIS 2.0. The solid blue line shows the piecewise linear profile used in the model. The nodes of the piecewise profile are marked with circles and are annotated with the parameter labels given in Equation 4. The five parameters $(\overline{M}, M_s, \zeta_M, H_{ML}, H_{MU})$ that define the function are annotated in green. The smooth red curve shows the hyperbolic tangent function (with different scale lengths above and below ζ_M) upon which the piecewise function is constructed.

$$
\begin{aligned}
M_0 &= \overline{M} & \zeta_{M,0} &= \zeta_M - 2H_{ML} \\
M_1 &= \frac{M_S + \overline{M}}{2} - \frac{M_S - \overline{M}}{2}\tanh(1) & \zeta_{M,1} &= \zeta_M - H_{ML} \\
M_2 &= \frac{M_S + \overline{M}}{2} & \zeta_{M,2} &= \zeta_M \\
M_3 &= \frac{M_S + \overline{M}}{2} + \frac{M_S - \overline{M}}{2}\tanh(1) & \zeta_{M,3} &= \zeta_M + H_{MU} \\
M_4 &= M_S & \zeta_{M,4} &= \zeta_M + 2H_{MU}
\end{aligned}
\tag{4}
$$

The mass profile is then defined as follows:

$$
M(\zeta) = \begin{cases} M_0 & \zeta \leq \zeta_{M,0} \\ M_i + (\zeta - \zeta_{M,i})a_{M,i} & \zeta_{M,i} \leq \zeta \leq \zeta_{M,i+1}; i = 0, 1, 2, 3 \\ M_4 & \zeta \geq \zeta_{M,4} \end{cases}
\tag{5}
$$

$$
a_{M,i} = \frac{M_{i+1} - M_i}{\zeta_{M,i+1} - \zeta_{M,i}} = \text{Slope of segment } i; i = 0, 1, 2, 3
$$

Figure 2 illustrates the global average effective mass profile for N_2. The theoretical basis for the approach is discussed in Picone et al. (2016). The choice of a piecewise linear effective mass profile allows the hydrostatic integral to be evaluated in closed form via integration by parts, as detailed in the supporting information (Text S1); in the Bates profile region, this requires the dilogarithm function, which we calculate using the algorithm described in Ginsberg and Zaborowski (1975).

The model assumes that the atmosphere is fully mixed below $\zeta_F = 70$ km, so that the effective mass is $\overline{M} = 28.96546$ amu for all species in that region. For N_2, O_2, Ar, and He, whose mixing ratios are well defined in the lower atmosphere, we compute an upper atmosphere reference density n_F in terms of mixing ratio and pressure, via the ideal gas law and hydrostatic balance:

$$
n_F = \Phi_F \frac{P(\zeta_F)}{kT(\zeta_F)}
$$

$$
\ln P(\zeta) = \ln P_0 - \frac{\overline{M}g_0}{k}\int_0^\zeta \frac{1}{T(\zeta')}d\zeta'; \quad \zeta \leq \zeta_F
\tag{6}
$$

Φ_F Mixing ratio of a particular species below ζ_F

$P(\zeta)$ Pressure

$P_0 = P(\zeta = 0)$ Pressure at surface

For O density below 85 km (where its production and loss are dominated by photochemistry), we substitute a linear combination of B-splines that is decoupled from the temperature:

$$
\ln n_O(\zeta) = \sum_{i=i_0}^{i_1} \beta_{O,i} S_i(\zeta); \ \zeta \leq \zeta_{SO} \ \text{(atomic oxygen only)}
$$

$n_O(\zeta)$ Number density of atomic oxygen

$\beta_{O,i}$ Coefficients on B-spline basis functions (fitting parameters)

$\zeta_{SO} = 85$ km   Transition height to hydrostatic profile (Equation 2)

The same spline nodes as the temperature profile (Equation 1) are used. At the joining height $\zeta_{SO} = 85$ km, C1 continuity is imposed, so that the last two spline coefficients are determined from the hydrostatic profile parameters (Equation 2). The O profile is defined down to a geopotential height of 50 km.
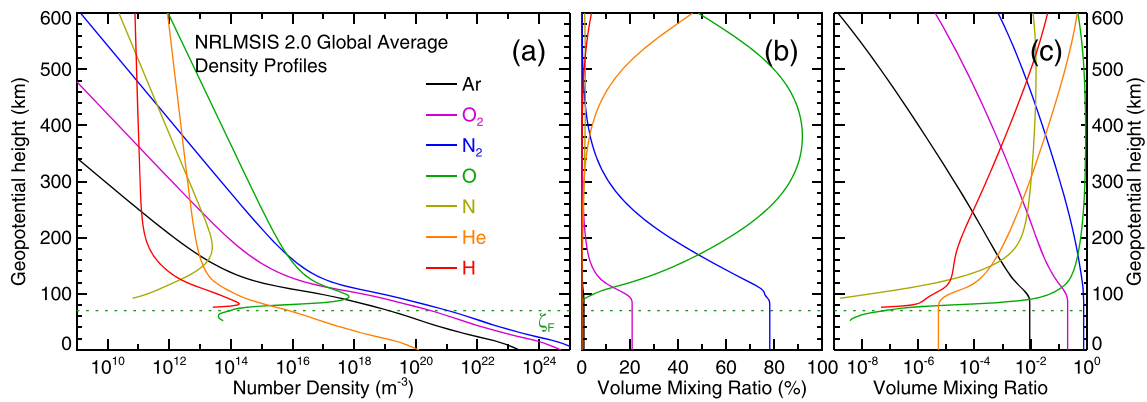
Figure 3. Global average density profiles in NRLMSIS 2.0. (a) Number density of Ar (black), O$_2$ (purple), N$_2$ (blue), O (green), N (yellow), He (orange), and H (red). (b) Volume mixing ratio of each species expressed as a percentage. (c) Volume mixing ratio on a log scale.

In summary, the model defines a density profile of a particular species in terms of up to 35 (possibly fitted and/or variable) parameters: 24 temperature parameters and 1 pressure parameter (which are common to all species); 1 mixing ratio or reference density; 3 mass profile parameters; and up to 6 correction parameters (C and R terms in Equation 2). The O profile additionally uses eight unconstrained spline coefficients between 50 and 85 km. Figure 3 shows the global average density and mixing ratio profiles for seven species represented by the model.

The major difference between the MSIS 2.0 species density profile and earlier versions is the treatment of the transition region (~70–200 km) between the fully mixed lower and middle atmosphere and the diffusively separated upper thermosphere. Earlier versions compute separate mixed and diffusive profiles, with the diffusive profile reference density defined at 120 km, then combine the two profiles using a geometric average (Hedin, 1987, Equation A12a). This decouples the thermosphere from temperature variations in the lower and middle atmosphere. In contrast, the effective mass profile in MSIS 2.0 couples, via the hydrostatic term in Equation 2, several species densities (N$_2$, O$_2$, He, and Ar) to the entire temperature profile and other species densities (O, H, and N) to the temperature profile down to reference altitudes in the mesosphere and lower thermosphere. Thus, in MSIS 2.0, species densities in the thermosphere are affected by temperature variations in the lower and middle atmosphere.

MSIS 2.0 eliminates the thermal diffusion term that in earlier versions was applied to He, Ar, and H. As discussed in Picone et al. (2016), the inclusion of thermal diffusion is not physically consistent with static composition profiles. Furthermore, we found that the effect of thermal diffusion in MSISE-00 is statistically unsupported by available He, Ar, and H data in lower and middle thermosphere, where vertical temperature gradients are sufficiently large for thermal diffusion to be active.

MSIS 2.0 and MSISE-00 both employ logistic function terms for dynamical corrections to species densities; in Equation 2, we express this term in terms of the hyperbolic tangent:

$$R\left[1 + \tanh\left(\frac{\zeta - \zeta_R}{H_R}\right)\right] = \frac{2R}{1 + \exp[-2(\zeta - \zeta_R)/H_R]} \tag{8}$$

However, in MSISE-00 and earlier versions, this term is used to produce specified mixing ratios near the turbopause, whereas in MSIS 2.0 this term is an upward projecting correction that represents departures from the hydrostatic/diffusive profile, such as winter bulges in the lighter species (e.g., Reber & Hays, 1973; Sutton, 2016). In MSIS 2.0, this term thus effectively takes on the role of the 120 km reference density in earlier versions, which represented such low frequency perturbations (Picone et al., 2013).

Earlier versions of MSIS use logistic function terms to represent chemical loss of O, H, and N and produce peaks in those species. MSIS 2.0 instead uses the simpler Chapman-like exponential term in Equation 2, which, unlike the logistic term, does not relax to a lower asymptote (earlier versions impose lower limits

of these species' profiles near or above the inflection point of their chemical loss logistic terms). MSIS 2.0 additionally extends the O profile down to 50 km using cubic B-splines (Equation 7).

MSISE-00 includes an anomalous oxygen component in the upper thermosphere, which nominally represents O^+ and hot O contributions to total mass density (Picone et al., 2002). This population is represented in the model with a separate, fixed temperature of 4000 K. We transferred the anomalous O component to the MSIS 2.0 model, accounting for the new geopotential height calculation but otherwise without modification.

2.4. Expansion of Vertical Profile Parameters

Each of the vertical temperature and density profile parameters is (or can be) expanded as a function of spherical harmonics in latitude and local time or longitude, solar zenith angle, harmonics in day of year, polynomials of the $F_{10.7}$ solar activity index (10.7 cm solar radio flux; Tapping, 2013), and a geomagnetic activity function. This expansion is largely the same as in MSISE-00 and earlier versions, as detailed in Hedin (1987, appendix, Equation A22). MSIS 2.0 introduces sigmoid terms in solar zenith angle (for day-night changes in mesospheric O and H) and a solar cycle modulation of the global annual and semiannual oscillations.

One important change in MSIS 2.0 is that the trigonometric terms in the expansion are split into their sine and cosine components (rather than the phase and amplitude parameters estimated in earlier versions for some of the variations). This linearizes the expansion with respect to the model parameters, facilitates the computation of the terms, and makes the parameter estimation process somewhat more robust. Some nonlinear terms have been retained from MSISE-00, including the solar cycle modulation of groups of variational terms, geomagnetic activity, UT terms, mixed UT/longitude, and mixed UT/longitude/geomagnetic activity terms.

The full expansion is detailed in the supporting information (Text S2). The expansion terms actually used for each vertical parameter and the parameter values are compiled in Data Set S1 in the supporting information.

3. Data

Table 1 summarizes the data sets and random samples we used to estimate the parameters of MSIS 2.0; acronym definitions are given at the end of the text. Most of the data are temperature measurements or reanalyses in the troposphere, stratosphere, mesosphere, and lower thermosphere. We also used mesosphere and lower thermosphere (MLT) O data from TIMED/SABER and Odin/OSIRIS, MLT H data from SABER, and orbit-derived upper thermospheric global average mass density data. In addition to these data, we also constructed synthetic MSISE-00 thermospheric data sets in order to relax the fits to the MSISE-00 thermosphere. In some cases, MSISE-00 thermospheric parameter values were directly mapped to the MSIS 2.0 formulation, as described in section 4.

To validate and analyze the model results, we used additional, independent random samples of the same data sets listed in Table 1. We also compared the model with middle thermospheric temperature data from Envisat/MIPAS and the Millstone Hill ISR, and with upper thermospheric mass density data from the CHAMP and GOCE accelerometers (see sections 6.4 and 6.5).

Brief descriptions of each data set are provided in section 3.1. The generation of random samples for fitting and validation is described in section 3.2. All of the data samples used to estimate the model parameters are available in the repository listed in the acknowledgments.

3.1. Data Sets

The temperature data sets listed in Table 1 are grouped into five measurement types: reanalysis, microwave, solar occultation, ground-based sodium (Na) Doppler lidar, and infrared. The O and H data sets are from infrared instruments, and the mass density data are derived from archived satellite and debris orbit data.

CFSR (Saha et al., 2010, 2014) is a reanalysis product of the National Centers for Environmental Prediction. It assimilates global meteorological data into an atmospheric model and outputs gridded atmospheric fields. CFSR version 1 (Saha et al., 2010) covers the years 1979–2011, and version 2 (Saha et al., 2014) covers the

Table 1
Summary of Data Sets and Samples Used to Estimate MSIS 2.0 Parameters

Data set or station/instrument	Latitude, longitude	Altitude (km)[a]	Local Time[b]	Years	No. Days[c]	No. Obs (10³)	Reference
				Temperature			
Reanalysis							
CFSR	90S–90N	0–30	0000–2,400	2002–2018	6,200	3,163	Saha et al. (2014)
MERRA2	90S–90N	0–55	0000–2,400	2002–2018	6,209	3,211	Gelaro et al. (2017)
Microwave							
Aura/MLS	82S–82N	10–85	0145, 1,345	2005–2014	3,589	4,940	Schwartz et al. (2008)
Solar Occultation							
ACE/FTS	85S–87N	15–102.5	Sunrise/set	2004–2013	2,436	5,068	Bernath (2007)
UARS/HALOE	77S–77N	37.5–102.5	Sunrise/set	2001–2005	880	2,769	Russell et al. (1993)
AIM/SOFIE	83S–89N	55–102.5	Sunrise/set	2007–2018	3,460	2,696	Marshall et al. (2011)
Na Doppler Lidar							
Andes	30S, 71 W	88–105	Night	2010–2014	51	645	Liu et al. (2016)
Boulder	40 N, 105 W	88–105	Night	2011–2014	198	240	Smith and Chu (2015)
Ft. Collins	41 N, 105 W	88–105	0000–2,400	1995–2010	804	244	Krueger et al. (2015)
Logan	42 N, 112 W	88–105	2010–2014	254	246	Krueger et al. (2015)
ALOMAR	69 N, 16E	88–105	Night	2003–2008	27	582	She et al. (2002)
Infrared							
TIMED/SABER	83S–84N	40–97.5	0000–2,400	2002–2016	5,060	5,817	Mertens et al. (2002)
Odin/OSIRIS	90S–90N	70–102.5	0650, 1850	2007–2012	1,848	1,808	Sheese et al. (2010)
				Atomic Oxygen			
TIMED/SABER	83S–83N	50–100	0000–2,400	2002–2013	3,964	3,058	Mlynczak, Hunt, Mast, et al. (2013), Mlynczak et al. (2013)
Odin/OSIRIS	90S–90N	75–100	0650, 1850	2007–2012	1,865	965	Sheese et al. (2011)
				Atomic Hydrogen			
TIMED/SABER	83S–83N	75–100	0000–2,400	2002–2013	3,963	3,751	Mlynczak et al. (2014)
				Mass Density			
Orbit-derived	Global Ave	400–575	Diurnal Ave	1986–2005	7,305	7,305	Emmert (2015a)

The numbers shown in this table refer to the fitting ensembles described in section 3.2. For temperature, O, and H data, the number of days and observations are the aggregate of all 15 ensembles.
[a]For temperature, the altitude ranges indicate the centers of the tapered probability distribution used to generate the samples. Otherwise, they indicate the discrete range of altitudes used in the fit.   [b]For sun-synchronous orbits, the approximate local times of equator crossings are given.   [c]Number of unique observation days in the sample.

years 2011 to present. We used CFSR temperatures from 2002 to 2018: 6-hourly output at universal times 0, 6, 12, and 18 hr, on a 0.5° latitude-longitude grid and a 37-level pressure grid (1,000 to 1 hPa).

MERRA2 (Gelaro et al., 2017) is a reanalysis product of NASA's Global Modeling and Assimilation Office that covers the years 1980 to present. We used MERRA2 temperatures from 2002 to 2018: 3-hourly output, on a 0.5° latitude × 0.625° longitude grid and a 72-level hybrid-eta grid (surface to 0.01 hPa).

MLS on the NASA Aura satellite (Waters et al., 2006) has been providing ~3,500 profiles per day of temperature, geopotential height, and a suite of trace gases since August 2004, from a sun-synchronous orbit. We used version 4.2 data (Livesey et al., 2017; Schwartz et al., 2008), which provides retrieved temperature on 42 fixed pressure surfaces (261–0.001 hPa), with temperature information coming primarily from the 118.75 GHz oxygen line. Vertical resolution in the mesosphere and lower thermosphere ranges from 6 to 13 km, becoming coarser with increasing altitude.

ACE/FTS is a high spectral resolution Fourier transform spectrometer (Bernath, 2007) that covers wavenumbers from 750 to 4,400 cm^{-1} (2.2 to 13.3 μm). ACE/FTS operates in solar occultation mode to provide altitude profiles of temperature, pressure, atmospheric extinction, and the volume mixing ratios for several dozen molecules. We used version 3.5 temperatures, which are given on a 1 km vertical grid from 0 to 150 km with a typical vertical resolution of about 3 km. The 15–102.5 km data used here are derived from the relative intensity of CO_2 lines.

UARS/HALOE recorded solar occultation measurements from October 1991 until its deactivation on 21 November 2005. The limb transmission measurements were used to infer profiles of temperature, as well

aerosol extinction and mixing rations of seven species (Russell et al., 1993). Temperatures from ~35 to ~85 km altitude were retrieved from CO_2 transmissions measured at 2.80 μm wavelength, using modeled CO_2 mixing ratio profiles in the forward simulations; the effective vertical resolution is ~3 km. Above ~85 km MSIS temperatures were appended, primarily to enable the NO channel retrievals. HALOE temperatures were validated by Harries et al. (1996) and McHugh et al. (2005), indicating agreement with correlative measurements to within the uncertainties for altitudes of ~35 to 75 km. We used version 19 temperature data.

AIM/SOFIE (Gordley et al., 2009; Russell et al., 2009) has operated from 2007 to present. SOFIE measurements at 16 wavelengths are used to retrieve temperature, as well as 5 species, polar mesospheric clouds, and meteoric smoke. SOFIE retrievals are reported on a 200 m vertical grid with an effective vertical resolution of 2 km. The version 1.3 SOFIE temperature retrievals used here (~55–100 km) are based on CO_2 transmission measurements at 4.32 μm (Marshall et al., 2011). SOFIE temperature validation reported by Stevens et al. (2012) and Hervig et al. (2016) indicate agreement with correlative measurements to within the uncertainties from ~30 to 95 km altitude.

The Na Doppler lidars listed in Table 1 share the same three-frequency Doppler lidar techniques summarized in Chu and Papen (2005) and references therein. Because of high collision rate, meteoric Na atoms in the mesosphere are believed to be in thermal equilibrium with the ambient atmosphere. By detecting the Doppler-broadened D2 absorption spectral line of Na atoms at three fixed frequencies and taking the ratios among the three-frequency returns, temperatures and winds in the MLT are inferred simultaneously from the Doppler broadened linewidth and the Doppler frequency shift. The development of Faraday-effect-based daytime filters enabled daytime measurements by several Na Doppler lidars (Arnold & She, 2003; Chen et al., 1996; Krueger et al., 2015; Smith & Chu, 2015).

The Andes Lidar Observatory (ALO) is located in Chile at the Cerro Pachon Mountain astronomy facility, which provides year-round clear viewing conditions (around 300 clear nights per year). The construction of the ALO building was funded by the University of Illinois at Urbana-Champaign. The ALO resonant Na wind/temperature lidar system (Liu et al., 2016) provides temperature profiles from 75 to 140 km altitude, with 1 min temporal resolution and 500 m vertical resolution.

The University of Colorado STAR Na Doppler lidar obtained very high-resolution data (Lu et al., 2015, 2017; Smith & Chu, 2015) at Table Mountain near Boulder, with the raw photon counts collected in resolutions of 3–9 s and 24 m. The effective temporal and vertical resolutions are 7.5 min and 0.96 km, respectively, for temperature profiles used in this paper, and the measurement uncertainties in the temperatures are ~0.3–1 K near the Na layer peak. The uncertainties in the winter months are usually smaller than those in the summer months due to the higher winter Na abundance.

The Na Doppler lidar at Ft. Collins, Colorado, operated from 1990 to 2010 and was relocated to Utah State University in Logan, Utah, in summer 2010, where it has been operating ever since. It measures the temperature and winds from ~80 to 105 km in full diurnal cycles (Krueger et al., 2015). The data used for this study have temporal and vertical resolution of 1 hr and 2 km, respectively.

The ALOMAR Na wind-temperature lidar operated from 2000 to 2017 at the Andøya Space Center as a U.S./Norwegian partnership (She et al., 2002). The lidar design was largely based on the Fort Collins Na lidar. Temporal and vertical resolutions are typically 2 min/1 km in the winter nighttime from 78 to 105 km and 15 min/2 km in summer daytime from 85 to 97 km. The data used in this study consist of 2003–2008 nighttime measurements averaged at 1 h and 1 km resolution.

TIMED/SABER is a limb scanning radiometer that records vertical profiles of infrared emission in 10 different spectral channels (Russell et al., 1999); it has operated from December 2001 to present. The specific channels on SABER enable a detailed assessment of the thermal structure, composition, and energy budget of the mesosphere and lower thermosphere (Mlynczak, 1996, 1997). In particular, SABER measures emission from carbon dioxide in the vicinity of 15 μm for the purpose of deriving kinetic temperature (Mertens et al., 2002). O and H are crucial to the derivation of the energy budget in the vicinity of the mesopause (Mlynczak & Solomon, 1993). SABER derives O and H densities using photochemical relationships specific to night and day (Mlynczak et al., 2013, 2014). SABER has a channel near 2.0 μm measuring emission from highly excited hydroxyl (OH) formed by the reaction of H and O_3 which is used in the derivation of H both day and night

and in the derivation of O at night. We used version 2.0 SABER T, O, and H data; a later version of nighttime O retrieval produces smaller peak densities (Mlynczak et al., 2018). Panka et al. (2018) also developed an algorithm for nighttime O that agrees well with Mlynczak et al. (2018). The updated nighttime O will be used in future MSIS development.

The Odin/OSIRIS optical spectrograph (McLinden et al., 2012) measures vertical profiles of 280–800 nm emissions from 7 to 110 km altitude with a vertical resolution of 2 km and a spectral resolution of 1 nm; it has operated from 2001 to present. Temperatures in the MLT are derived from the O_2 A-band emission (Sheese et al., 2010). Daytime O density is inferred iteratively in conjunction with O_3 using a photochemical forward model of the A-band emission (Sheese et al., 2011). Nighttime O density is derived from A-band emission associated with O recombination (Sheese et al., 2011). Odin is in a sun-synchronous orbit; the equator crossings of the temperature and O data occur near 0700 and 1900 local time.

The orbit-derived thermospheric mass density data consist of daily, global average mass density at altitudes from 250 to 575 km (Emmert, 2009, 2015a). The data cover the years 1967–2013 and are derived from two-line orbital element sets (TLEs) on ~5,000 objects (we also denote this data set as "TLE densities"). Following Weimer et al. (2018) and based on the ballistic coefficient estimates of Pilinski et al. (2011), we reduced the values in this data set by 7%. For MSIS 2.0, we used 1986–2005 data for fitting and the remaining years for validation.

The following data sets were not used to estimate the MSIS 2.0 model parameters but are used for independent comparison and analysis in section 6.

The Millstone Hill UHF ISR system (42.6 N, 288.5E, Apex magnetic latitude 54°) has been in operation since 1963. It provides observations of altitudinal profiles of several plasma parameters, including ion temperature, that are determined from the received signal power and spectrum; neutral temperature between 100 and 180 km altitude is derived from the ion temperature (Salah & Evans, 1973). An average ion mass of 31 amu is assumed at altitudes below 130 km, and an ion composition model is used above this altitude. Observations below ~180 km are limited to mostly daytime hours because of the low electron density at night. Availability of data below ~180 km greatly increased after 2002, when improved software radar design patterns (Grydeland et al., 2005) were implemented. We used all available lower and middle thermospheric neutral temperatures from 2002 to 2015: 311,000 observations (at 4 km altitude intervals) taken on 748 unique days.

Envisat/MIPAS measured spectrally resolved 5.3 μm nitric oxide limb emissions in the lower and middle thermosphere in its upper atmospheric observation mode during 2006–2012, from which kinetic temperatures and nitric oxide concentrations are jointly derived (Bermejo-Pantaleón et al., 2011). We used all available version 622 temperature observations in the 105–170 km altitude range: a total of 1.86 million observations (at 5 km altitude intervals) taken on 334 days. The Envisat orbit was sun-synchronous, and the equatorward crossings of the MIPAS observations occurred near 1,015 and 2,215 local time.

CHAMP and GOCE total mass density data were derived from satellite accelerometer measurements, by making use of satellite aerodynamic and geometry models (Doornbos et al., 2010; March et al., 2019). The CHAMP data cover the time period January 2001 to September 2010; we used a random sample of 1.19 million observations on 1,926 days, excluding the anomalous solar minimum years 2005–2009. CHAMP was in a near-polar orbit with an inclination of 87°.The GOCE data cover the time period November 2009 to October 2013; we used a random sample of version 2.0 data consisting of 0.84 million observations on 1,227 days. GOCE was in a near-sun-synchronous orbit with equator crossings near 0700 and 1900 local time.

3.2. Sampling Procedure

From the temperature data sets listed in Table 1, we assembled 30 random samples or ensembles. We used the first 15 ensembles for fitting via sequential estimation and the second 15 for validation. For the fitting ensembles (1–15) we additionally imposed tapered altitude restrictions on each data set, in order to avoid regions where a given data set is systematically biased relative to the other data sets (some examples are discussed in section 6.1) or is near the limits of reliability of the data set. The taper, which is intended to avoid sharp statistical gradients in the fitting procedure, was implemented via a hyperbolic tangent probability function with a scale height of 2.5 km. The altitude ranges given in Table 1 denote the centers of the
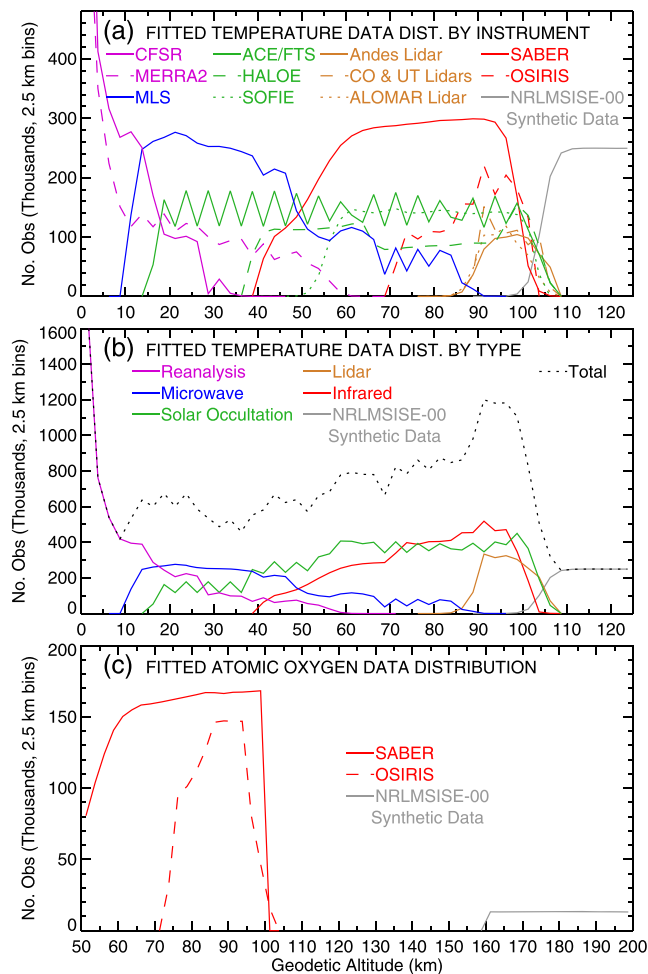
Figure 4. (a) Altitude distribution of sampled temperature records used in fitting MSIS 2.0, by instrument type. Shown are the numbers of randomly selected observations in 2.5 km bins. The sample of the three Colorado and Utah lidar data sets is combined into one curve. Also shown is the distribution of MSISE-00 synthetic data used to anchor the fit. (b) Same as (a) but grouped by instrument type. The dotted line shows the total number of sampled observations in each 2.5 km bin. (c) Altitude distribution of fitted SABER and OSIRIS atomic oxygen data, along with synthetic upper thermospheric MSISE-00 O data used in the fit.

lower and upper tapers; the fitted reanalysis samples extend all the way down to the ground with no lower taper. Note that the validation ensembles (16–30) include some additional data outside these height ranges.

Figure 4a shows the distribution of all the temperature data in the fitting ensembles (ensembles 1–15) as a function of altitude in 2.5 km bins; Figure 4b shows the same distributions but grouped by instrument type. The relative sizes of the samples were chosen subjectively, in order to obtain a balance among instruments and measurement types. Because there are no major discrepancies among the data sets (see section 6.1), the model results are not sensitive to the relative sample sizes. The distributions in Figure 4 represent the weight of each data set's or group's contribution to the model: In the fitting process, each of the sample observations is weighted equally. Figure S1 further illustrates the distribution of the upper mesospheric fitting ensembles as a function of local time and latitude.

We gave SABER the most weight in the mesosphere, in part because its full local time coverage is important for capturing tides. Where the three occultation data sets overlap (above ~60 km), we gave them approximately equal weight, except that we excluded HALOE observations poleward of 45° between 65 and 95 km, in order to avoid possible contamination by polar mesospheric clouds. The lidar sample is approximately evenly allocated among the three regions where the five instruments are located: Chile, Colorado/Utah, and Norway. In the upper mesosphere, the infrared, lidar, and occultation measurements have roughly equal weight. In the stratosphere, the Aura/MLS measurements are the largest component of the sample, and the reanalysis products provide almost all the data in the troposphere.

The random selection process did not exclude duplicates, so some observations will appear more than once in a given ensemble or across ensembles. For large data sets the statistical influence of duplicates is negligible. For small data sets the duplicates increase the influence of underrepresented measurement techniques. The total number of fitted observations for each data set is listed in Table 1, along with the number of unique days in the sample.

To generate the MSISE-00 synthetic data in each fitting ensemble, we randomly selected a set of measurement dates and times from the constituent data sets and random locations on the sphere. We then evaluated MSISE-00 at those times and locations on a fixed altitude grid (2 km intervals from 90 to 130 km). In this way, the MSISE-00 data represent the same mix of solar activity, geomagnetic activity, and day-of-year conditions as the measurements.

We followed a similar procedure to generate 30 random ensembles of the O data sets and 30 random samples of the H data sets. For the fitting ensembles (1–15), the data were restricted to the altitude ranges listed in Table 1, without any tapering. The validation ensembles (16–30) include additional data slightly outside these ranges. Synthetic MSISE-00 data were added to the fitting ensembles as described above, except that they were evenly distributed over 160–500 km altitude for O and 300–500 km for H. Figure 4c illustrates the altitude distribution of the combined O fitting ensembles. The SABER H data are approximately evenly distributed over the 75–100 km interval.

4. Model Parameter Estimation Procedure

In this section, we describe the procedure we used to set and/or estimate the MSIS 2.0 model parameters. Some parameters are set a priori, some are ported from MSISE-00, and some are tuned to the fitting

ensembles and/or MSISE-00 synthetic data. Many of the vertical parameters are not expanded beyond their global values, and some are expanded only sparsely. The final parameter values are tabulated in Data Set S1, which can be consulted to determine which variations the model contains. There are 3,306 nonzero parameter values in MSIS 2.0, compared to ~1,300 in MSISE-00.

4.1. Constant, A Priori Parameters

As discussed in section 2.1 and the appendix, MSIS 2.0 uses the WGS-84 reference ellipsoid and a reference gravity value $g_0 = 9.80665$ m/s^2 to calculate geopotential height and in Equation 2. For the effective mass profiles (Equations 3–5) and the lower atmospheric mixing ratios (Equation 6), we used the values in Picard et al. (2008): dry-air mean mass $\overline{M} = 28.96546$ Da in the fully mixed region and species masses and mixing ratios of N$_2$, O$_2$, Ar, and He. We computed species masses of O and N by halving the N$_2$ and O$_2$ masses, and we set the mass of H to 1.0 Da.

For the three remaining effective mass profile parameters (transition height and lower and upper scale heights), we used values derived from MSISE-00 global average profiles (with thermal diffusion and chemical/dynamical corrections turned off). For N$_2$, we additionally ported the MSISE-00 turbopause height seasonal-latitudinal variation and applied it to the transition height of the MSIS 2.0 N$_2$ effective mass profile. Otherwise, the effective mass profiles do not vary with location or geophysical conditions.

The global average surface pressure P_0 in Equation 6 was set so that the modeled lower tropospheric pressure matches the global average of the reanalysis data sets (CFSR and MERRA2), after subtracting out the water vapor partial pressure from the latter (MSIS is currently a dry-air model). The surface pressure in MSIS 2.0 does not vary around $P_0 = 1002.692$ hPa.

We set the chemical/dynamical correction reference heights and scale heights (ζ_R, H_R) to fixed values subjectively chosen to smoothly represent upper thermospheric departures from the terms in equation 2. Currently available data are insufficient to statistically constrain these parameters. The amplitudes of the chemical/dynamical correction terms were set or estimated in subsequent steps described in this section.

4.2. Linear Fit of Temperature up to 122.5 Km

After setting the constants a priori parameters, we estimated the 24 temperature spline coefficients (α_i in Equation 1) and selected expansions via a linear, ordinary least squares fit to data ensembles 1–15. The spline domain extends up to 122.5 km geopotential height, whereas the fitting data extend only up to ~105 km. The MSISE-00 synthetic data anchored the fit over this data gap. The selected expansion includes latitude, day of year, local time, and longitude dependences; other variations were estimated in subsequent steps. Because the spline part of the temperature component is purely linear with respect to the model parameters (for the selected expansion), this fitting step is carried out via an iterative direct full matrix inversion (cf. Drob et al., 2015).

4.3. Merge Linear Temperature Fit With MSISE-00 Thermospheric Parameters

Next, the MSISE-00 Bates temperature parameters (T_{ex}, T_B, T_B' in Equation 1) and their expansions were mapped to the MSIS 2.0 formulation. We then combined the linearly fitted spline parameters with the Bates parameters to form the full MSIS 2.0 temperature construction. In this process, the top three spline parameters from the linear fit are essentially replaced with the Bates parameters, which determine those three spline coefficients via the continuity constraint. The MSIS 2.0 temperature component thus consists of the MSISE-00 thermosphere and a new lower and middle atmosphere tuned to contemporary (mostly post-2000) data. The MSIS 2.0 temperature between ~122.5 and 200 km cannot exactly match MSISE-00, due to the differences in the geopotential height formulation that slightly affect the gradient and shape of the Bates profiles. The temperature differences between MSIS 2.0 and MSISE-00 in this region are less than ~5 K and peak near 150 km, which is negligible compared to model uncertainty at these altitudes.

4.4. Subsequent Refinement of Temperature Parameters With Fitting Ensembles

With the linear fit, we found that the sun-synchronous data (MLS, OSIRIS, and the occultation data sets) introduced spurious semidiurnal variations below ~80 km. Therefore, we refined the semidiurnal tidal parameters with these data excluded. This tuning was conducted on the full model via unweighted, Levenberg-Marquardt chi-square minimization (using ODRPACK95; Zwolak et al., 2007); although the retuned

parameters are linear coefficients, this nonlinear estimation algorithm is more robust to tuning selected parameters while holding others constant. We tuned the semidiurnal parameters using each of the 15 fitting ensembles (without the sun-synchronous data) in sequence, with the parameters derived from one ensemble used as the starting estimate for the next ensemble. For the final parameter estimates, we computed the average of the parameters derived from ensembles 6–15 (i.e., omitting the results from the first five "spin-up" ensembles).

Next, we extended the solar activity dependence of the temperature parameters down to ~70 km (in MSISE-00, only the three Bates parameters and the temperature at 110 km vary with solar activity). We again used the 15 fitting ensembles (this time with all data sets) sequentially and averaged over the results from ensembles 6–15. The solar activity terms in the model are global; that is, they are not modulated by latitude or other variables. This is the last stage of the temperature parameter estimation process.

4.5. Tune Species Densities to MSISE-00 Thermosphere

The initial species density profiles are defined by the temperature profile and the fixed mixing ratio and effective mass profile parameters described in section 4.1. For O, H, N, and anomalous O, we supplied initial guesses of the global average reference density and chemical loss term parameters; for O, we initially set its spline coefficients to a global, uniform value. We then tuned the chemical/dynamical correction amplitudes, and the chemical loss parameters of N and anomalous O, to approximately match MSISE-00 in the upper thermosphere.

4.6. Tune O and H Data to Fitting Ensembles

Next, we tuned the O and H parameters using the 15 fitting ensembles for each species described in section 3.2. The fitting ensembles include synthetic MSISE-00 upper thermospheric data, so that the MSISE-00 thermosphere is approximately preserved while improving O and H in the mesosphere and lower thermosphere. As with the temperature tuning, we sequentially applied the ODRPACK minimization algorithm to each of the ensembles and then averaged the parameters estimated with ensembles 6–10. We found that the parameter estimates converged quickly within the first five ensembles, with little variation among ensembles 6–10.

4.7. Tune Upper Thermospheric O to Orbit-Derived Mass Density Data

Finally, we further tuned the global intra-annual variation (annual and semiannual) of upper thermospheric O to the 1986–2005 orbit-derived mass density data set listed in Table 1 (the mass mixing ratio of O is ~60–95% between 400 and 575 km). This adjustment also includes a new modulation by solar activity, which is motivated by the results of Bowman et al. (2008) and Emmert and Picone (2010).

Except for this adjustment to O, the modeled upper thermospheric densities approximately match MSISE-00; the difference is generally less than 10%. The upper thermospheric MSIS 2.0 O densities are ~10% less overall than MSISE-00, as a result of the tuning to the orbit derived data. Additionally, the N_2 chemical/dynamical correction (see section 2.3), which was tuned to match upper thermospheric MSISE-00 N_2 densities, is turned off by default in the MSIS 2.0 software, for reasons discussed in section 6.4.

5. Statistical Comparisons of Models to Data

In this section, we summarize statistical verifications that we conducted on MSIS 2.0 using the independent data ensembles (16–30) described in section 3.2, independent time intervals from the orbit-derived thermospheric mass density data set, and CHAMP and GOCE thermospheric mass density data. Following the approaches used for MSISE-00 (Picone et al., 2002), two statistical metrics of the data-minus-model residuals are computed: the mean (which we also refer to as the bias) and the standard deviation. We computed these metrics for each data set and in selected altitude bins. For density quantities, we computed the residuals in natural log space (i.e., ln [data/model]), so that a residual of 0.1 corresponds to a data-minus-model difference of ~10%. The bias indicates systematic differences between a data set and the corresponding model estimates, while the standard deviation indicates the agreement between the geophysical variations in the data and model (it also includes measurement noise).

One of our goals in constructing and tuning MSIS 2.0 was to produce a model that statistically performs at least as well as MSISE-00 and better in most instances (i.e., smaller biases and residual standard deviations).

Table 2
Residual Standard Deviations by Instrument, in Four Broad Altitude Bins

Data set/station/instrument	75–100 km MSISE-00	75–100 km MSIS 2.0	50–75 km MSISE-00	50–75 km MSIS 2.0	25–50 km MSISE-00	25–50 km MSIS 2.0	0–25 km MSISE-00	0–25 km MSIS 2.0
			Temperature residual std. dev. (K)					
CFSR			2.6	3.0	5.4	5.3	4.7	4.1
MERRA2	11.0	9.3	8.1	6.6	5.8	5.1	4.7	4.1
Aura/MLS	9.1	10.1	7.3	6.6	5.9	5.3	5.0	4.5
ACE/FTS	12.0	10.3	9.5	7.9	8.3	7.6	5.6	5.5
UARS/HALOE	12.2	9.8	10.3	8.1	6.3	5.8		
AIM/SOFIE	12.9	11.2	9.7	8.6	9.7	9.2		
Andes Lidar	23.1	20.5						
Boulder Lidar	28.9	28.0						
Ft. Collins Lidar	15.1	14.0						
Logan Lidar	15.0	13.7						
ALOMAR Lidar	15.8	14.2	10.4	10.0				
TIMED/SABER	18.2	15.4	9.7	8.1	6.1	5.7		
Odin/OSIRIS	15.0	13.4	9.4	7.7				
			$\ln(n_O)$ residual Std. Dev.					
TIMED/SABER	1.23	0.91		0.88				
Odin/OSIRIS	1.50	0.97		1.35				
			$\ln(n_H)$ residual std. dev.					
TIMED/SABER	4.29	0.76						

This was accomplished by the assimilation of extensive new data sets in the lower and middle atmosphere and by largely retaining the MSISE-00 thermosphere. Further development of the MSIS thermosphere will be the subject of future work. We computed the statistical metrics with respect to both MSISE-00 and MSIS 2.0 and compared their values.

Table 2 shows residual standard deviations, of the independent ensembles with respect to MSISE-00 and MSIS 2.0, in four broad altitude bins in the mesosphere and below. In almost all cases, the standard deviations with respect to MSIS 2.0 are smaller, indicating that MSIS 2.0 is capturing the geophysical variability in the data better than MSISE–00. The MSIS 2.0 residual standard deviation values are typically 10–15 K in the upper mesosphere (75–100 km), 6–8 K in the lower mesosphere (50–75 km), and 5–6 K in the stratosphere and troposphere. The MSIS 2.0 standard deviations are typically 1–2 K smaller than MSISE-00 in the mesosphere and ~0.5 K smaller in the stratosphere and troposphere. The only two instances in which the MSISE-00 residual standard deviations are smaller occur at the upper altitudinal extent of the Aura/MLS and CFSR data sets, where these data are presumably less reliable (these data sets also show biases relative to the other data sets at their upper extent, as shown in the next session, and data from such regions were excluded from the fitting ensembles for that reason).

The MSIS 2.0 residual standard deviations of O and H in the mesosphere are large (~0.9 ≅ a factor of 2) but are much smaller than with MSISE-00. MSISE-00 does not output O below 72.5 km, so MSIS 2.0 sets a new performance benchmark for O in this region.

More detailed results in 5 km altitude bins, including the bias statistic, are provided in Data Sets S2 (temperature), S3 (O density), and S4 (H density).

Data Set S5 contains residual statistics of the orbit-derived mass density data set. The tuning of upper thermospheric O in MSIS 2.0 (section 4.7) resulted in lower residual standard deviations than MSISE-00 not just in the 1986–2005 interval used for fitting but also in the independent 1971–1985 interval; the residual standard deviations during 2006–2013 are considerably larger with both MSISE-00 and MSIS 2.0, due to the anomalous solar minimum that occurred during this period (Emmert et al., 2014). The MSIS 2.0 mass densities are ~10% lower than MSISE-00, as a result of the recalibration of the MSISE-00 thermosphere to the downward revised orbit-derived density. Tuning to a later epoch (1986–2005) may have also contributed, due to observed long-term trends in density (e.g., Emmert, 2015a).

Data Set S6 contains residual statistics of the CHAMP and GOCE accelerometer-derived mass density data. Above 400 km, the residual standard deviation is lower with MSIS 2.0 than with MSISE-00, further indicating that the tuning of the global inter-annual variation is robust.

6. Scientific Results and Technical Issues

An important aspect of the model generation and validation process is the examination of data-model biases as a function of altitude and other geophysical variables. As mentioned in section 5, the mean residual statistic indicates systematic differences (i.e., biases) between a data set and the corresponding model estimates. By extension, this metric also indicates biases *among* data sets, with the model acting to filter out common spatiotemporal geophysical variations, provided that (1) the model accurately captures the average variations or (2) the data sets sample approximately the same geophysical conditions. We also discuss some scientific and technical issues that arose during the development of the model and which are illustrative of the state of knowledge of the structure and average behavior of the atmosphere, particularly in the mesosphere and thermosphere.

6.1. Temperature and Pressure in the Mesosphere and Below

Figure 5 shows average data-minus-model temperature residuals as a function of altitude from the ground to 105 km. The data are from the validation ensembles (16–30) described in section 3.2. It is evident from the plots that the mean residuals with respect to MSIS 2.0 (right column) are flatter than those with respect to MSISE-00 (left column), indicating that MSIS 2.0 better captures the overall height dependence of the data. The residuals with respect to MSISE-00 tend to be negative by up to ~10 K, except for the reanalysis data between 5 and 15 km altitude. This indicates that contemporary data in the stratosphere and mesosphere are colder than MSISE-00, which is based on tabulated data from the 1970s and 1980s (Hedin, 1991). This shift is qualitatively consistent with studies of long-term trends in these regions (e.g., Garcia et al., 2019; Laštovička, 2017; Randel et al., 2016).

The mean residuals from the various temperature data sets are generally within ~3 K of each other, suggesting that there are no major systematic biases among the data sets. Exceptions are as follows. The Na lidar data tend to become increasingly warmer than the other data sets below ~85 km, by up to ~40 K (Figure 5d). SABER temperatures above the high-latitude summer mesopause (~90 km) are up to ~50 K warmer than the other data sets (Figure 5b). The CFSR data begin to deviate from the other data sets above ~35 km, and the MERRA2 data deviate strongly above ~70 km. In all of these cases, the outlying data were excluded from the fitting ensembles via the altitude selection described in section 3.2. Additionally, Aura/MLS data between 55 and 95 km are ~4 K cooler than the other data sets, as is MERRA2, which assimilates MLS data.

Figure 6 shows contours of MSIS 2.0 zonal mean temperature as a function of latitude and altitude (left column), as well as the change from MSISE-00 (right column). As mentioned above, MSIS 2.0 is warmer overall than MSISE-00 in the upper troposphere and cooler overall in the stratosphere and mesosphere. Regions where MSIS 2.0 is warmer include the low- and middle-latitude upper mesosphere (particularly during winter) and the high-latitude lower mesosphere (particularly during winter). Presumably, the difference patterns are a consequence of the average differences between the ~2002 and 2018 data assimilated into MSIS 2.0 and the 1970s and 1980s data on which MSISE-00 is based. The pattern of the annual average change from MSISE-00 to MSIS 2.0 is similar to the ~1974 to 2003 change modeled by Solomon et al., 2018; Figure 1); some of the differences are likely attributable to the fact that Solomon et al. presented their results as a function of log-pressure not altitude as in Figure 6.

Figure 7 highlights the high-latitude summer mesopause region in more detail; Figure S2 contains additional bin-averaged plots of high-latitude mesopause region data and corresponding MSIS 2.0 results, as a function of day of year. Höffner and Lübken (2007) noted that potassium lidar measurements from Spitsbergen (78°N), taken during 2001–2003, showed a colder and higher summer mesopause minimum than MSISE-00 (119 K vs. 132 K and 90 km vs. 88 km). The MSIS 2.0 summer minimum at 78°N is 126 K (Figure 7d), which is closer to the Spitzbergen lidar results, but the height of the mesopause is still lower, at ~87 km. The SABER and OSIRIS measurements show a mesopause height of ~90 km at this latitude (Figure 7b), which agrees with Höffner and Lübken (2007). At 69°, both the infrared and occultation data
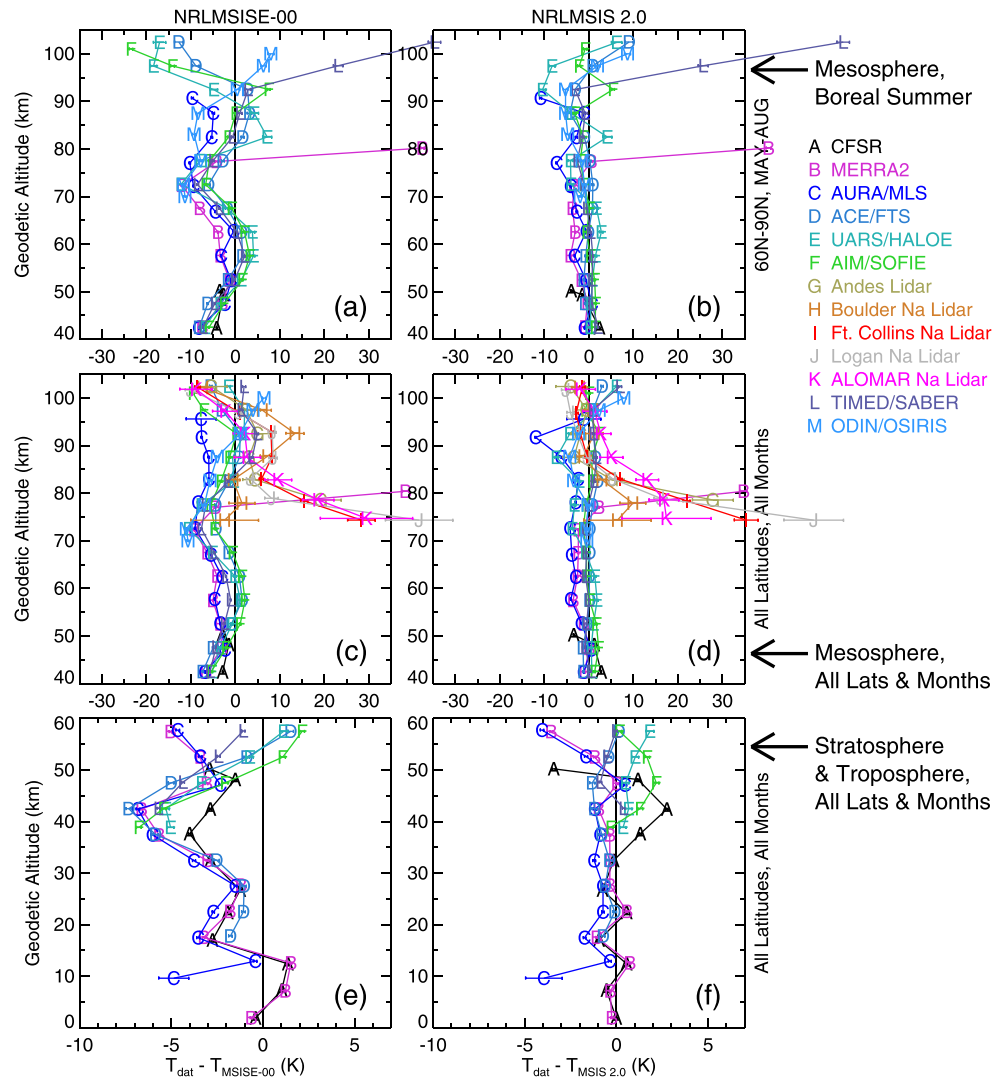
Figure 5. Mean data-minus-model residuals of the temperature validation ensembles as a function of altitude, with respect to MSISE-00 (left column: [a, c, e]) and MSIS 2.0 (right column: [b, d, f]). Panels (a) and (b) show mesospheric results for the boreal summer (above 60°N latitude, May–August; panels (c) and (d) show mesospheric results for all latitudes and months, and panels (e) and (f) show stratospheric and tropospheric results for all latitudes and months (note the different x axis scale for these panels). Results from the different data sets are denoted by the letters and colors indicated in the legend; these symbols are reused in subsequent plots. Error bars denote the 1σ estimated uncertainty of the mean (standard deviation divided by the square root of the number of unique days in the sample).

sets indicate a lower mesopause at 87–88 km, and here MSIS 2.0 is in better agreement with the data (Figure 7a), including daytime ALOMAR Na lidar data not used in the MSIS 2.0 fit (cf. Figure S3 with Figure 7c). This latitude dependence of the summer mesopause height was also noted by Höffner and Lübken (2007), who cited Lübken's (1999) analysis of falling sphere measurements at 69°N.

Capturing this shift in mesopause height with latitude would require additional expansion terms in MSIS; MSIS 2.0 includes zonal mean Legendre function terms up to degree 6. Additionally, the region above the summer mesopause contains the strongest vertical temperature gradients in the atmosphere, as the temperature transitions from a summer minimum in the mesosphere to a summer maximum in the thermosphere. This gradient is largely controlled by the Bates parameter T'_B (Equation 1), which in MSIS 2.0 is taken from MSISE-00 and includes only low-resolution variations as a function of latitude and day of year. More flexibility in this parameter could improve the model's representation of the high-latitude summer
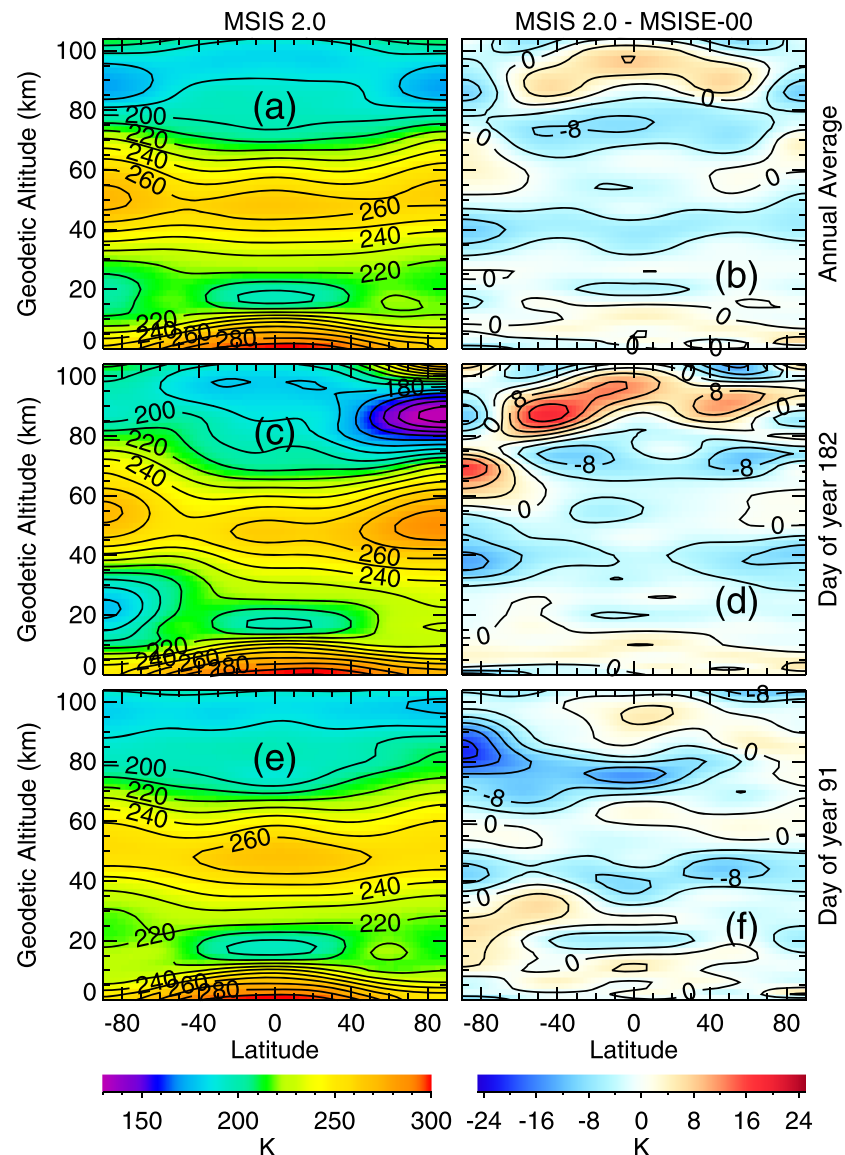
Figure 6. (left column) Zonal mean temperature structure of MSIS 2.0 as a function of latitude and altitude; the contour interval is 10 K. (right column) Zonal mean temperature difference between MSIS 2.0 and MSISE-00; the contour interval is 4 K. Shown are annual average conditions (a, b), June solstice (day 182, c, d), and March equinox (day 91, e, f). Results are shown for solar activity condition $F_{10.7} = 150$.

mesopause, provided there are sufficient data near the inflection point (~120 km altitude) to constrain its value.

Figure S4 shows average data-minus-model temperature residuals as a function of local time in selected altitude and latitude bins. As with the altitude dependence shown in Figure 5, the local time dependence of the mean residuals with respect to MSIS 2.0 are flatter than those with respect to MSISE-00, indicating that MSIS 2.0 better captures the migrating tides in the data. Figure S5 compares the local time variation of the absolute measured and modeled temperatures near 95 km at middle and low latitudes, further demonstrating the improved tides in MSIS 2.0. Figure 8 illustrates the mesospheric local time-latitude structure in the two models, after subtracting out zonal means. At 95 km, MSISE-00 shows a primarily semidiurnal pattern with a single peak near the equator, whereas MSIS 2.0 exhibits a mix of diurnal and semidiurnal variations with two peaks at ~40°S and 40°N. At 70 km, MSISE-00 shows a highly structured semidiurnal variation during June solstice and a weak diurnal variation during equinox; the local time variation in MSIS 2.0 at this altitude is relatively weak in both seasons (<5 K).
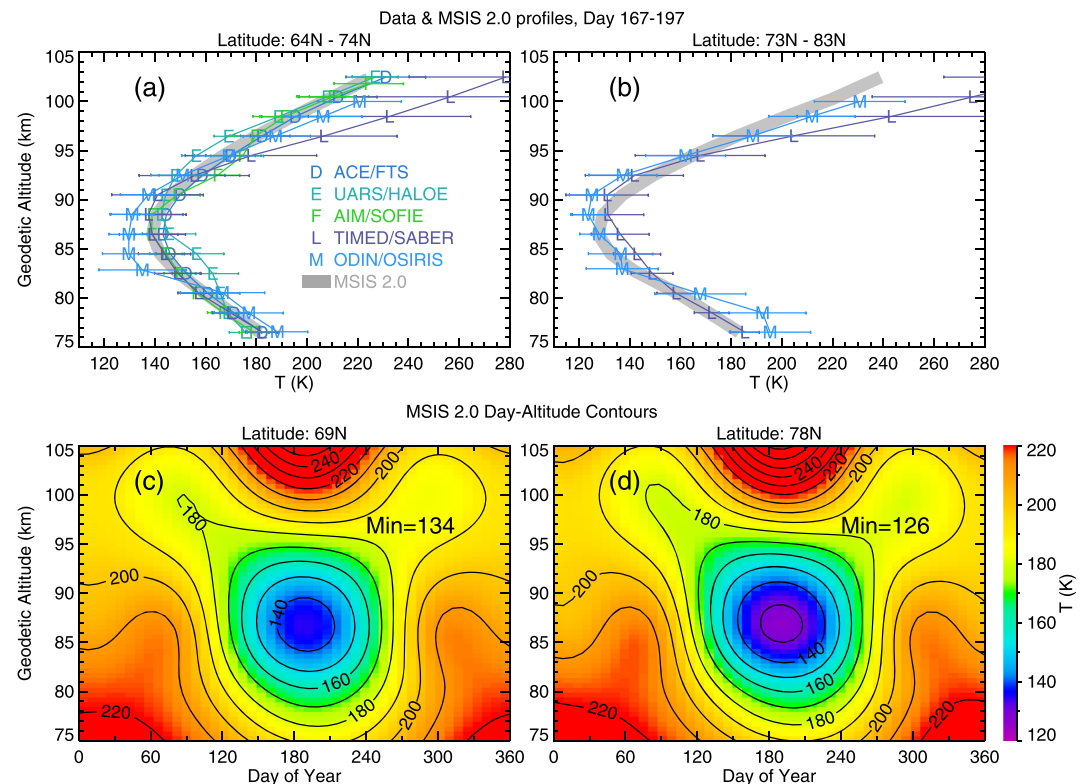
Figure 7. (a, b) Average temperatures (from the validation ensembles) in the summer mesopause region as a function of altitude, in 2 km bins. Results are shown for the 30 days surrounding June solstice (Days 167–197) and latitudes 64–74°N (a) and 73–83°N (b). Error bars indicate the standard deviation of the data in each bin. The thick gray curve shows corresponding averages from MSIS 2.0. (c, d) Day-altitude contours of zonal mean MSIS 2.0 temperatures at 69°N and 78°N. Results are shown for solar activity condition $F_{10.7} = 150$. The contour interval is 10 K.

Figure 9 shows mean residuals of log-pressure from the reanalysis, after subtracting out the water vapor partial pressure from the data. The residuals with respect to MSISE-00 become increasingly negative above 15 km as a result of the lower temperatures in the data (see Figure 5) that imply a more contracted atmosphere. The residuals with respect to MSIS 2.0 are largely flat and mostly less than 2%, indicating that the overall pressure structure in the MSIS 2.0 lower and middle atmosphere is consistent with the reanalyses. The bias near the surface is zero by design (see section 4.1) but then shifts to +1.1% above 5 km. This is because the dry-air MSIS atmosphere has a smaller-scale height in the lower troposphere than the moist-air reanalyses (the presence of water vapor decreases the mean molecular mass; the lighter air is more expanded in altitude, resulting in higher partial pressures of all species at a given altitude). The residual standard deviation of the log-pressure residuals with respect to MSIS 2.0 is ~1.3% near the surface, increasing to ~5.5% in the lower mesosphere (not shown).

6.2. Atomic Oxygen

For upper atmospheric applications, O is perhaps the most important and the most challenging species to represent. O is the dominant neutral constituent in the atmosphere at thermospheric altitudes and is the primary source atom for the F region ionosphere. However, in the MLT region, O is a minor constituent and sensitive to photochemical production and loss, dynamical transport, and diffusion (e.g., Jones et al., 2014, 2017; Smith et al., 2010; Swenson et al., 2019). Furthermore, these processes that determine the MLT O distribution vary over a wide range of spatiotemporal scales. MSISE-00 and earlier version provided an accurate representation of thermospheric O from mass spectrometer data but did not include any global satellite measurements for O in the MLT region. Rather, several rocket profiles were used to extrapolate the O profiles into the middle atmosphere and provide an estimate for the value of the O peak in the MLT. Not surprisingly, significant differences between MSISE-00 and the newer MLT satellite data sets have been
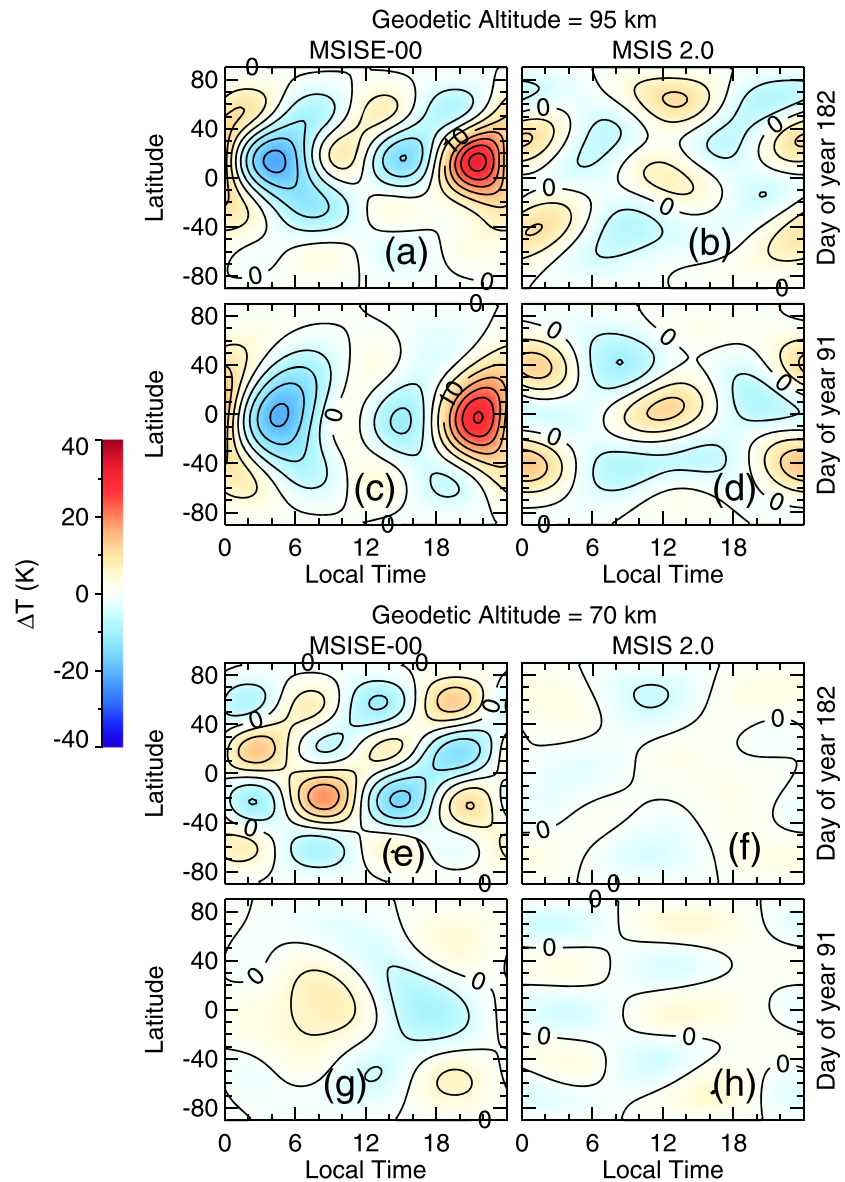
Figure 8. Modeled temperature variations as a function of local time and latitude, after subtracting out zonal means. Results are shown for MSISE-00 (left column) and MSIS 2.0 (right column), at altitudes of 95 km (a–d) and 70 km (e–h) and at June solstice (first and third rows) and March equinox (second and fourth rows). The contour interval is 5 K.

reported. For example, Sheese et al. (2011) suggested caution when using MSISE-00 for MLT O if one wants accuracy to better than an order of magnitude. By incorporating SABER and OSIRIS O data within the MLT region, MSIS 2.0 significantly ameliorates those earlier issues and provides a seamless representation of O from 50 km through to the upper thermosphere.

Figure 10 shows mean residuals of log O density measurements from SABER and OSIRIS, as a function of altitude. With respect to MSISE-00, the OSIRIS mean residuals are within 0.2 (~22%) of zero, and the SABER mean residuals are ~0.3–0.6 (35–82%) larger than OSIRIS. Below 80 km, the MSISE-00 O density falls off much more rapidly than the measurements, so the mean residuals of both data sets are very large. With respect to MSIS 2.0, the difference between the OSIRIS and SABER mean residuals is smaller, ~0.2–0.3 (22–35%), suggesting that MSIS 2.0 is accounting for some O variations that affect the mean residual via differences between the OSIRIS and SABER sampling patterns (e.g., sun-synchronous vs. precessing). Other comparisons, such as with SCIAMACHY (Kaufmann et al., 2014; Zhu & Kaufmann, 2019), have suggested
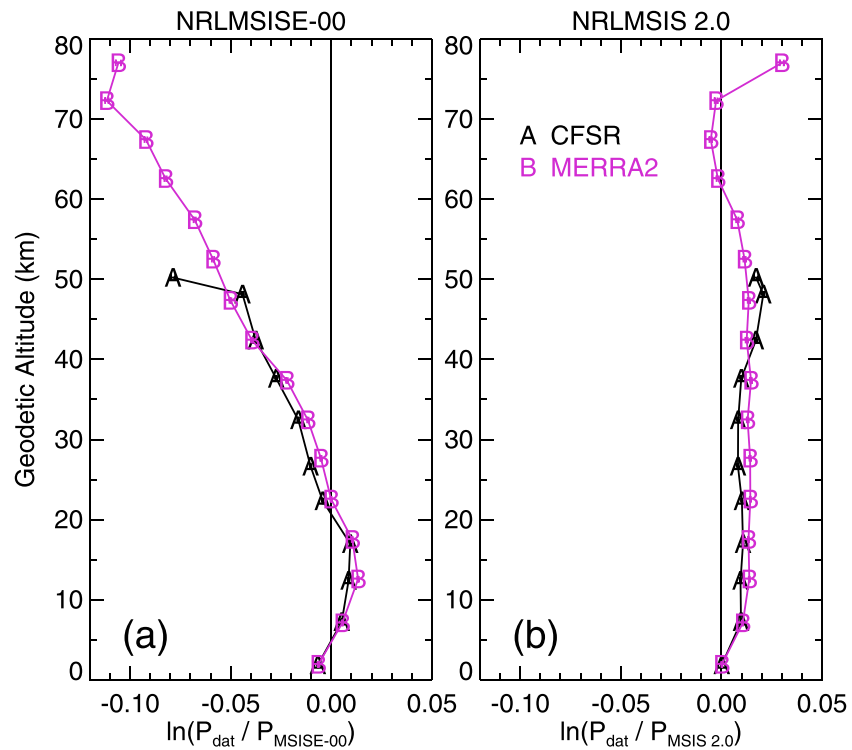
Figure 9. Mean data-minus-model residuals of log-pressure from the reanalysis data sets as a function of altitude in 5 km bins, with respect to (a) MSISE-00 and (b) MSIS 2.0. The water vapor partial pressure was subtracted from the data prior to computing residuals. Error bars (very small) denote the 1σ estimated uncertainty of the mean.
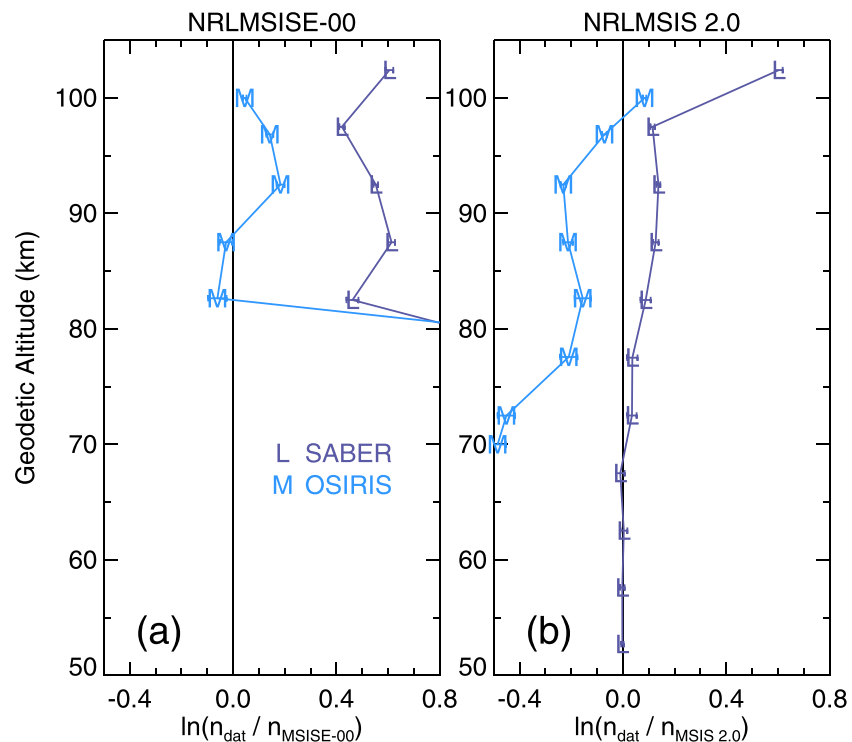

Figure 10. Mean data-minus-model residuals of log O density as a function of altitude in 5 km bins, with respect to (a) MSISE-00 and (b) MSIS 2.0. Error bars denote the 1σ estimated uncertainty of the mean.
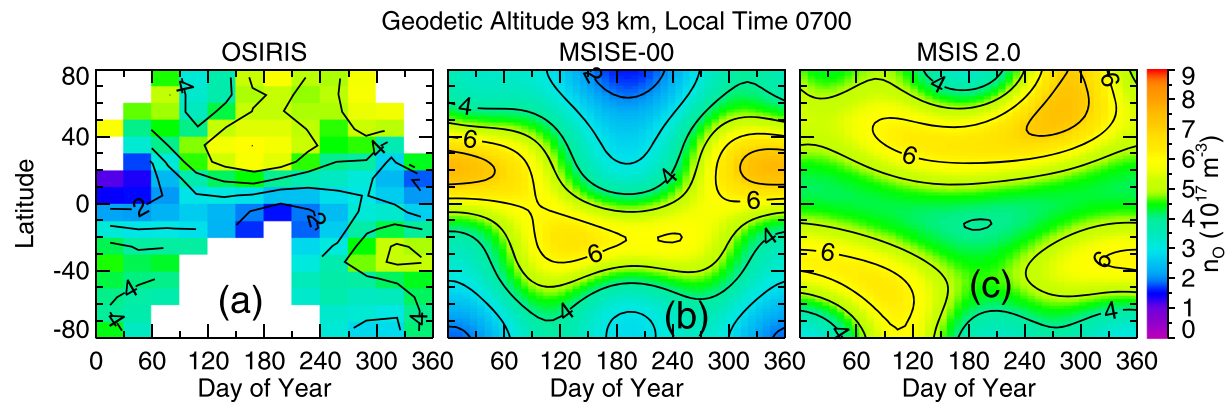
Figure 11. (a) Binned averages of OSIRIS O observations (from the validation ensembles) at 93 km altitude in the 0700 local time sector, as a function of day of year (30.5 days bins) and latitude (10° bins). (b, c) Corresponding results from MSISE-00 and MSIS 2.0, respectively. The contour interval is 10^{17} m^{-3}.

that SABER is too high by about 30%. Mlynczak et al. (2018) discussed how modifications to the OH(v') kinetics scheme could lessen the biases and produce a consistent global energy budget. Above 75 km, MSIS 2.0 falls between the SABER and OSIRIS data but leans more toward SABER, as a result of the weighting shown in Figure 4c. Below 70 km, where there is no OSIRIS data, MSIS 2.0 follows the SABER data closely, on average.

Figure 11 is an update to Figure 12 of Sheese et al. (2011), who pointed out major discrepancies in the seasonal-latitudinal variation of MSISE-00 (we note that the Sheese et al. figure showed results for 0700 local time, not 1900 as indicated in their caption). Figure 11 shows that MSIS 2.0 properly captures the equatorial minimum and semiannual oscillation seen in OSIRIS. At midlatitudes MSIS 2.0 now yields an annual variation with the same phase (summer maximum) as the OSIRIS observations. At northern polar latitudes, while improved relative to MSISE00, MSIS 2.0 still does not fully capture the summer maximum seen in OSIRIS, but it is not clear if this is a significant feature of the OSIRIS data. At southern polar latitudes, OSIRIS does not show a clear summer maximum, and MSIS 2.0 is in better agreement with OSIRIS than in the north.

Figure 12 illustrates the seasonal dependence of midlatitude O profiles from SABER, OSIRIS, MSISE-00, and MSIS 2.0. MSIS 2.0 exhibits a narrower and larger summer O peak than MSISE00. A larger peak during summer is consistent with the SABER and OSIRIS data (and with Figure 11); the narrower peak follows from the seasonal phase reversal to larger winter O density in the upper thermosphere. The SABER data do not form a well-defined peak in summer: The SABER values near 95 km are larger than MSIS 2.0, and these values extend upward to 105 km with little or no gradient. This feature of the SABER data is possibly associated with daytime overestimation of O_3 at these altitudes; a corrective scheme is currently under development. SABER data above 100 km were excluded from the MSIS 2.0 fit.

During winter, MSIS 2.0 and MSISE-00 show a very similar structure at the peak, but MSIS 2.0 is greater by almost an order of magnitude near 80 km. Above ~105 km, MSIS 2.0 and MSISE-00 are fairly similar with MSIS 2.0 O values smaller by ~10%, as a result of tuning to upper thermospheric mass density data (see section 4.7).

Figure 13 compares the local time dependence of SABER and OSIRIS O with MSIS 2.0, at selected altitudes in the MLT. As one moves downward into the mesosphere, O transitions from being under dynamical control to under photochemical control. O photochemistry is driven by rapid daytime photolysis of ozone followed by rapid recombination after sunset. This midmesospheric diurnal variation has previously been analyzed and discussed by Siskind et al. (2015). MSIS 2.0 includes diurnal harmonics and a solar zenith angle transition function to represent the transition from dynamical control to photochemical control. At 65–70 km (Figure 13d), the model very accurately represents the day-night differences. At 75–85 km (Figures 13c and 13b), the SABER data begin to show a rounded daytime local time dependence suggesting the growing influence of transport; MSIS 2.0 captures this feature, although the model densities are ~50% smaller than SABER and ~30% smaller than OSIRIS in the postdawn sector. Near the O peak at 93–98 km (Figure 13a), there is no clear local time dependence in the data. As noted above, the SABER summer density near the peak is larger than both MSIS 2.0 and OSIRIS.
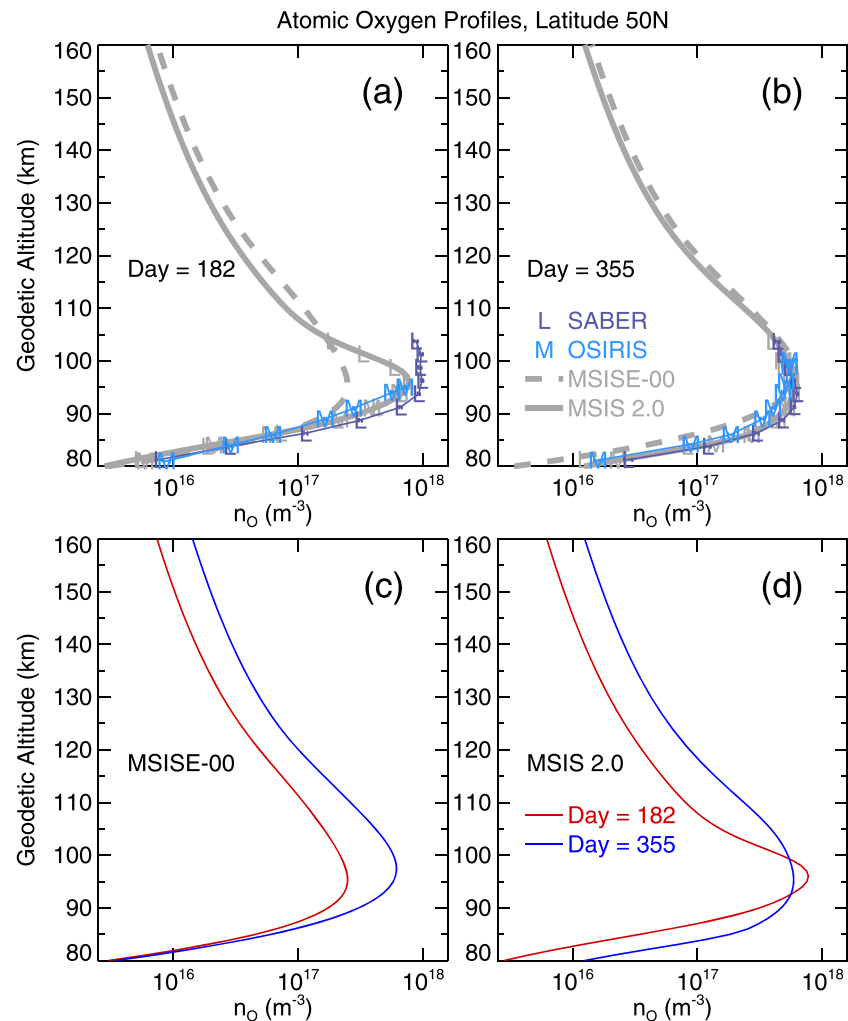
Figure 12. (a) Binned averages of SABER (purple L's) and OSIRIS (blue M's) $\log_{10}$ O density (from the validation ensembles) as a function of altitude (2.5 km bins) in a 60 day bin surrounding June solstice (day 182) and a 20° latitude bin centered on 50°N; data from all local times were combined. Corresponding point-for-point MSIS 2.0 averages are shown using the same letters but in gray (e.g., gray L's for SABER). The gray solid line shows the diurnally averaged MSIS 2.0 profile at Day 182, latitude 50°N, $F_{10.7} = 150$, $Ap = 4.0$; the gray dashed line shows the corresponding MSISE-00 profile. (b) Same as (a) but for December solstice (Day 355). (c) Comparison of the summer (red) and winter (blue) MSISE-00 profiles shown in (a) and (b). (d) Same as (c) but showing the MSIS2.0 summer and winter profiles.

6.3. Atomic Hydrogen

With the inclusion of SABER H data, MSIS 2.0 provides a more accurate description of hydrogen variability in the MLT than MSISE-00 (see Table 2 and Data Set S4) One important aspect of this variability is the reversal from a summer maximum at the mesopause (cf. Siskind et al., 2018) to a winter maximum in the upper thermosphere, commonly referred to as the "winter bulge" (Keating & Prior, 1968). Consistent with the known variability of light species, MSISE-00 does have a winter maximum in the upper thermosphere but has very little seasonal variation in the MLT region (Qian et al., 2018). Figure 14 illustrates the improved seasonal variation by comparing MSISE-00 and MSIS 2.0 in a format similar to Figure 5 of Qian et al. (2018). The figure shows binned averages of the SABER data and corresponding MSIS profiles extending from the mesosphere to the upper thermosphere. Both SABER and MSIS 2.0 show a Northern Hemisphere summer maximum (Southern Hemisphere results, not shown, are very similar) in the MLT; MSIS 2.0 has a winter maximum in the upper thermosphere that it inherited from MSISE-00. The crossover altitude is about 150 km, in approximate agreement with the WACCM-X results presented by Qian et al. (2018). However,
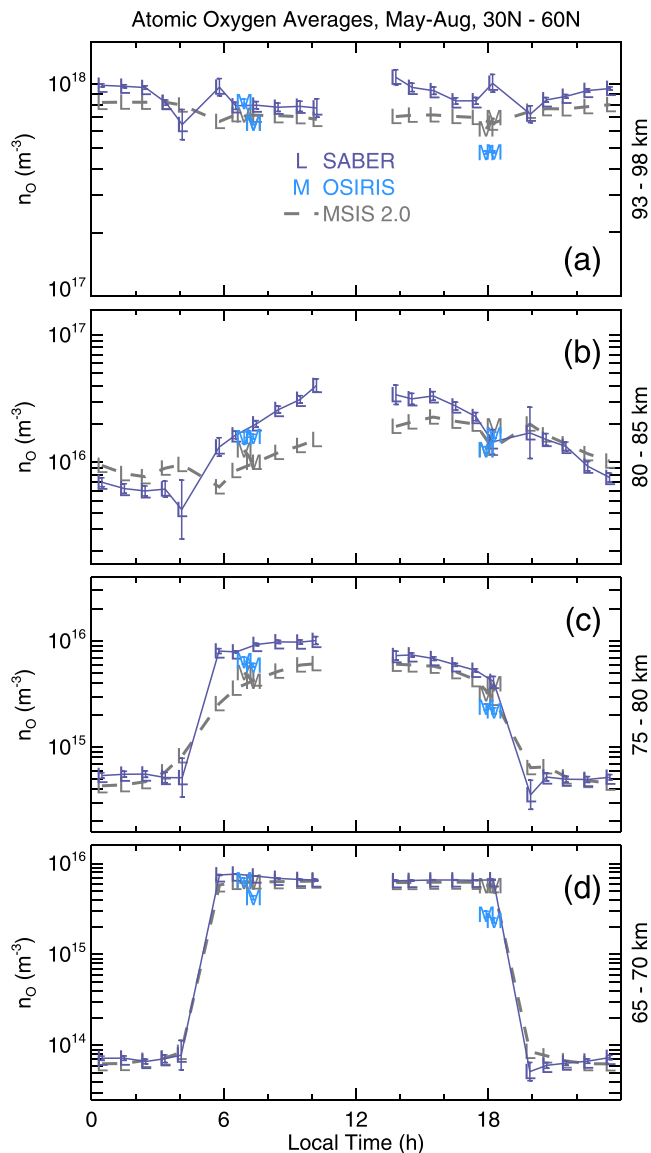
Figure 13. (a) Binned averages of SABER (purple L's) and OSIRIS (blue M's) log10 O density (from the validation ensembles) as a function of local time (1 hr bins) during northern midlatitude summer (30–60°N, May–August). Corresponding point-for-point MSIS 2.0 averages are shown using the same letters but in gray (e.g., gray L's for SABER). Results are shown for the altitude bins indicated to the right of each panel.

there is currently no data available to accurately determine where this crossover occurs, which underscores the need for global neutral constituent measurements between 100 and 300 km.

An interesting aspect of the SABER data discussed by Mlynczak et al. (2014) is the inverse relationship between MLT H and solar activity. Mlynczak et al. (2014) ascribe this difference to relative roles of decreasing temperatures with decreasing solar activity and changes in the O/O_3 ratio. Qian et al. (2018) point out that this solar cycle change was present in MSISE-00 at all altitudes above 80 km, but not in WACCM-X, which showed an alternating positive-negative-positive effect between 80 and 130 km. The solar cycle variation in MSIS 2.0 is generally consistent both with MSISE-00 and SABER and differs from the WACCMX results shown by Qian et al. (2018). This is shown in Figure 15, which presents solar minimum and maximum averages and their differences. The SABER and MSIS 2.0 differences (Figure 15b) are consistently negative at all altitudes above 80 km.

6.4. Middle Thermosphere Temperature and Composition

Although several new middle and upper thermospheric temperature data sets have become available since MSISE-00 was developed, we found that there is considerable variation among their mean residuals with respect to MSISE-00. Thermospheric species and mass densities are highly sensitive to the entire thermospheric temperature profile, and any temperature adjustments to the model need to be consistent with observed density residuals (such as accelerometer-derived mass densities). With some data sets, the mean temperature residuals show strong local time and/or latitude dependences that are not evident in available density data. On the other hand, available density data are insufficient to constrain the thermospheric temperature profile. Because of these issues, we chose to largely retain the MSISE-00 thermosphere in MSIS 2.0 and to defer a major thermospheric upgrade until we can accurately reconcile the various historical thermospheric temperature and density data sets, ideally with new measurements that can constrain the problem. In this section, we explore some of the aspects of this challenge.

There are few contemporary data sets of middle thermospheric (~120–200 km) temperature. Figure 16 shows mean residuals, with respect to MSIS 2.0, of Envisat/MIPAS and Millstone Hill ISR temperatures as a function of altitude. Because the MSIS 2.0 thermospheric temperature above 120 km is largely identical to MSISE-00, the results are nearly the same if MSISE-00 is used as the reference model. Nighttime MIPAS and daytime Mil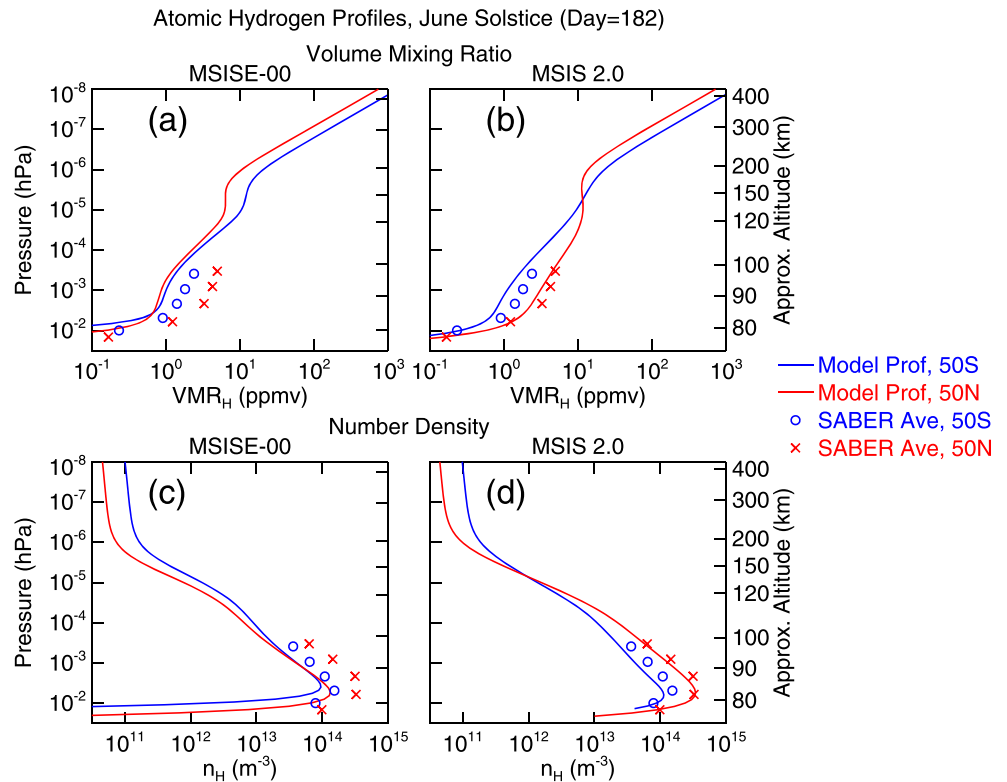lstone Hill ISR data (Figures 16b and 16a, respectively) suggest that MSIS temperatures are 30–50 K too high above 120 km, which may be associated with long-term trends that have been reported in the ISR data (Zhang et al., 2011; Zhang & Holt, 2013). However, daytime MIPAS average temperatures (Figure 16a) are within 10–20 K of MSIS 2.0. Thus, the daytime MIPAS and ISR residuals differ by up to 30 K. The biases depend on altitude, and the MIPAS and ISR profile shapes are different. These biases appear minor from a total temperature profile perspective (Figure 16d), but they strongly affect middle and upper thermospheric density via thermal expansion or contraction: A 30 K decrease in temperature above 120 km produces an ~25% decrease in mass density at 400 km. Height-dependent biases are not necessarily problematic, since they can possibly be corrected by tuning the Bates profile parameters, and the Bates profile is not an exact representation of thermal balance. However, the MIPAS and ISR mean residuals appear to be discontinuous with those of the upper mesospheric data sets (which are tightly clustered within ~5 K near their upper bound of 105 km), and it is not immediately clear how this discontinuity should be resolved.

Figure 14. (a) Binned averages of SABER H volume mixing ratios as a function of pressure level (derived from 5 km altitude bins) near June solstice (Days 152–212) in summer (red x's, 45–55°N) and winter (blue circles, 55–45°S). The dashed lines show corresponding point-for-point binned averages from MSISE-00. The solid lines show MSISE-00 zonal mean profiles evaluated at the center of the season and latitude bins and for $F_{10.7} = 150$ and $Ap = 15$. (b) Same as (a) but showing MSIS 2.0 results. (c, d) Same as (a, b) but showing log number density.

Figure 17 similarly shows MIPAS and Millstone Hill ISR mean residuals as a function of local time. Near 120 km, the ISR residuals are fairly consistent over local time and in different seasons. Between 150 and 180 km, however, the ISR residuals depend strongly on local time and season, and the MIPAS nighttime residuals also depend strongly on season. It may be possible to tune MSIS to better match these patterns, but this would require commensurate tuning of the MSIS species densities, since these bias patterns are not evident in accelerometer measurements of upper thermospheric mass density.
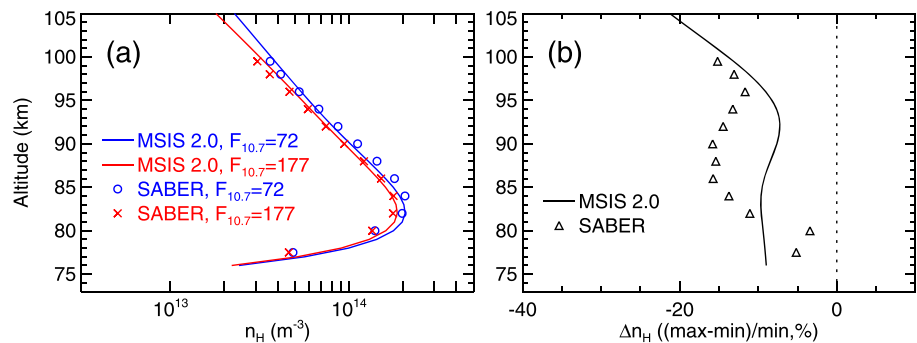

Figure 15. (a) Binned averages of SABER H log number density as a function of altitude (2 km bins) for solar minimum (blue circles 81 day average $F_{10.7} < 80$) and solar maximum (red x's, 81 day average $F_{10.7} > 150$). The solid lines show corresponding global average MSISE-00 profiles for the average solar activity conditions in each bin (72, 177). (b) The average relative difference between the profiles in (a).
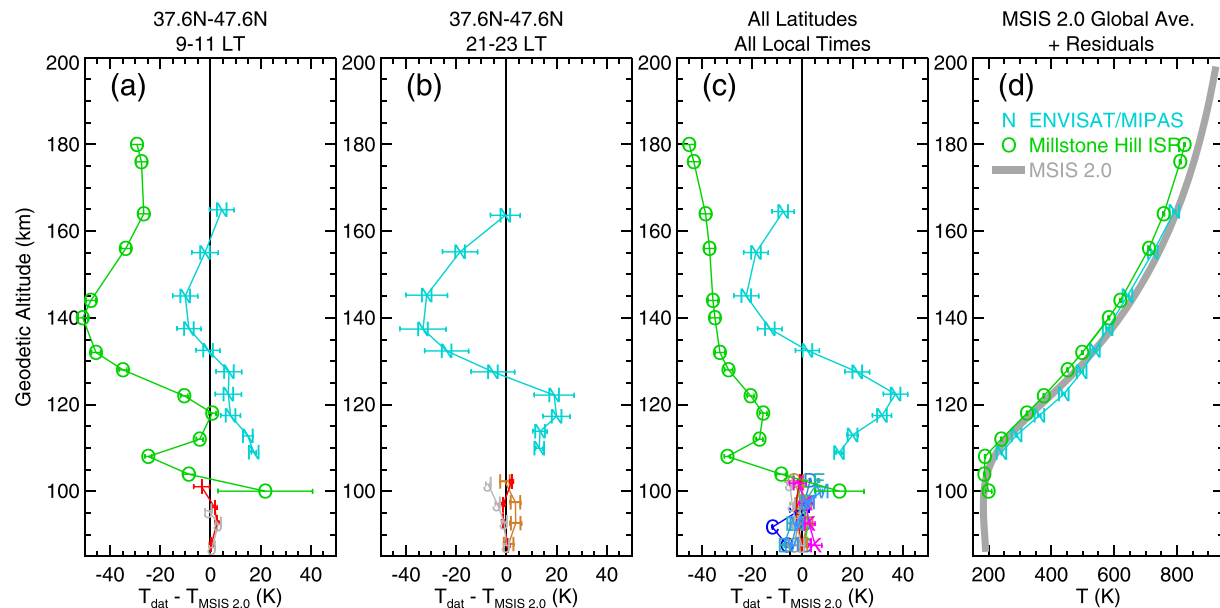
Figure 16. (a) Mean data-minus-model residuals of the lower and middle thermospheric temperature measurements from Envisat/MIPAS ("N") and Millstone Hill ISR ("O"), as a function of altitude (5 km bins below 140 km, 10 km bins above), with respect to MSIS 2.0. Results are shown for a 10° latitude bin surrounding the Millstone Hill location and a 2 hr local time bin surrounding the morning portion of the Envisat sun-synchronous orbital plane. Below 100 km, corresponding results from the same data sets used in Figure 5 are shown, using the same symbols as Figure 5 legend. Error bars indicate the 1σ estimated uncertainty of the mean. (b) Same as (a) but showing results for the nighttime MIPAS data. (c) Same as (a) but including data from all local times and latitudes. (d) MSIS 2.0 global average temperature profile (solid gray line) plus the MIPAS and Millstone Hill ISR residuals shown in (c).

We note here that MSISE-00 assimilated 1988–1997 Millstone Hill ISR temperatures between 100 and 130 km altitude, which may account for the relatively flat mean residuals in Figures 17d–17f (which are based on 2002–2015 ISR data). However, the MSIS thermospheric temperature profile and variations are also strongly determined by mass spectrometer measurements, from the 1970s and 1980s, of N_2 density. This reliance on density data to estimate thermospheric temperature resulted in accurate middle and upper thermospheric N_2 density, but it did not distinguish the contribution of lower-altitude temperatures to the N_2 density, which in MSISE-00 and earlier versions was effectively encoded in a poorly resolved combination of the reference thermospheric N_2 density at 120 km and the Bates temperature and gradient at 120 km.

The cooler stratospheric and mesospheric temperatures in MSIS 2.0 (section 6.1), compared to MSISE-00, have direct and strong implications for thermospheric N_2 density. In MSIS 2.0, thermospheric N_2 density is now coupled to the underlying temperature via the effective mass profile. Figure 18 shows the difference between the MSIS 2.0 and MSISE-00 global average temperature profiles and the resulting change in the N_2 density profile. Although the temperature change is relatively small, the effect of the thermal contraction accumulates with altitude via the hydrostatic term in Equation 2. The resulting MSIS 2.0 thermospheric N_2 density is ~20% lower than MSISE-00. This result is not sensitive to the choice of effective mass profile parameters, because the mass shift of N_2 is quite small (28.97 to 28 Da). Thus, even without new data in the thermosphere, the highly robust lower and middle atmosphere temperature data constrain the N_2 density in the thermosphere. Other thermospheric species, especially O_2, Ar, and He, are likely also affected by the cooler stratospheric and mesospheric temperatures, but in the absence of middle thermospheric data to constrain their effective mass profile parameters (to which the densities are much more sensitive than in the case of N_2), the thermospheric densities of these species remain uncertain, and in MSIS 2.0 they relax to MSISE-00.

For users who desire the legacy thermospheric N_2 profile and its variations, the software includes an option to turn on the relaxation to MSISE-00. For the global average profile, this relaxation is illustrated by the dashed line in Figure 18c. A consequence of turning this adjustment on is that the model becomes hydrostatically imbalanced between ~120 and 200 km, due to the added N_2 mass, as shown in Figure 18d. This panel shows the gradient of model pressure with respect to geopotential height divided by mass density, which is
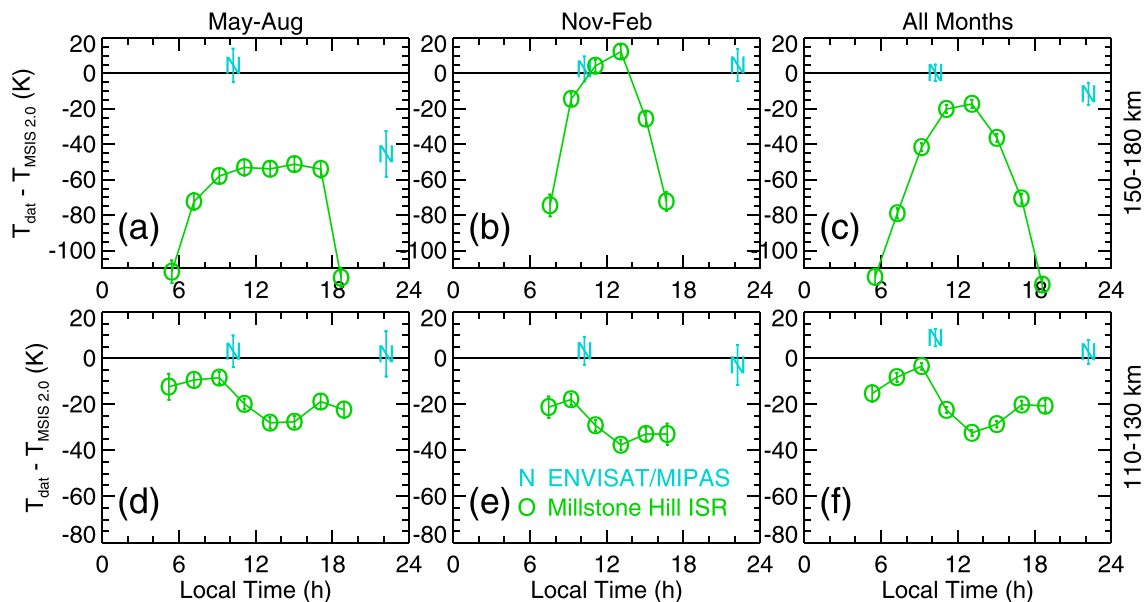
Figure 17. Binned average MIPAS and Millstone Hill ISR residuals with respect to MSIS 2.0 as a function of local time (2 hr bins). Results are shown for a 10° latitude bin surrounding the Millstone Hill location. Error bars indicate the 1σ estimated uncertainty of the mean. (a–c) The 150–180 km altitude. (d–f) The 110–130 km altitude. (a, d) June solstice months (May–August). (b, e) December solstice months (November–February). (c, f) All months combined.

equal to the reference gravitational acceleration if the model is in hydrostatic equilibrium. Both MSISE-00 and MSIS 2.0 are hydrostatically balanced in the fully mixed region below 70 km and the diffusive equilibrium region above ~200 km. In the transition region, imbalances are typically less than 0.1 m/s^2; with the legacy N_2 adjustment turned on, the imbalance is ~0.4 m/s^2.

Empirical models of the thermosphere are sometimes referred to as "static" models (e.g., Jacchia, 1971), because the parameters of these models (including MSIS 2.0) are fixed and the formulations do not include explicit time dependence. However, the results discussed in this paper and studies of atmospheric trends (e.g., Garcia et al., 2019; Laštovička, 2017; Randel et al., 2016; Solomon et al., 2018) demonstrate that the climatological behavior of the thermosphere and underlying layers is not stationary. This poses additional challenges for the MSIS thermosphere, since its thermospheric composition is based primarily on mass spectrometer data that are now 35–50 years old, and available contemporary data consist mainly of in situ mass density measurements, which, while highly valuable, do not by themselves resolve the influences of temperature and individual species dynamics. Ultraviolet remote sensing of N_2, O_2, and O densities above 130 km (Meier et al., 2015) is a relatively new and promising technique, but there are some outstanding discrepancies between those retrievals and mass density derived from orbital drag (e.g., Emmert et al., 2014, Figure 17). Further complicating the challenge of updating the MSIS thermosphere is that measurement techniques often use MSIS itself as an initial guess or for ancillary parameters needed in the retrieval (e.g., Bermejo-Pantaleón et al., 2011; Meier et al., 2015).

We also note that species densities in the middle thermosphere are not known to the accuracy needed to fully understand the critical transition from a fully mixed atmosphere to a diffusively separated one. In physics-based models, subgrid-scale mixing parameterizations typically have to be tuned to produce the observed upper thermosphere (e.g., Qian et al., 2009). Observations needed to constrain lower and middle thermospheric physics are scarce, and the 100–200 km region can perhaps be termed the new "ignorosphere," an epithet previously applied to the mesosphere, which by comparison is now well measured and understood. The lack of 100–200 km observations is due in part because it is a difficult region to probe: Emissions that can be exploited by remote sensing are relatively weak, and orbital in situ access is hampered by large satellite drag.

Considering these challenges, we judge that advances in climatological specification of the thermosphere would be greatly facilitated by (1) new in situ mass spectrometer measurements of species densities to recalibrate the thermosphere to the current epoch; (2) new techniques for, and extensive measurements of,
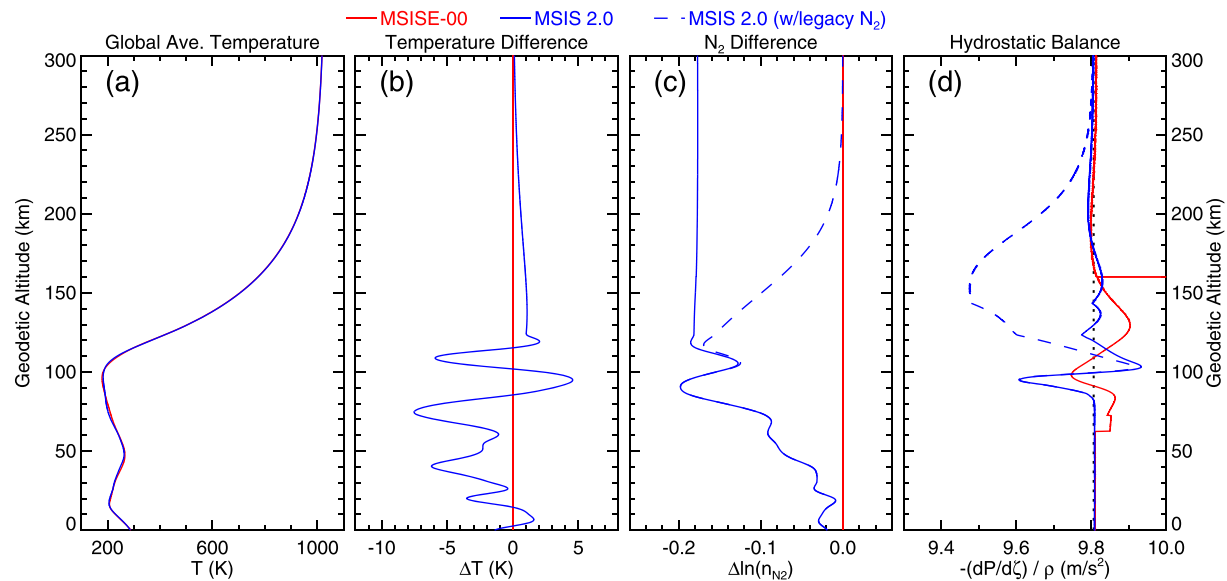
Figure 18. Examination of hydrostatic balance in MSISE-00 and MSIS 2.0. (a) Global average temperature profiles from MSISE-00 (red) and MSIS 2.0 (blue). (b) Temperature difference with respect to MSISE-00. (c) Difference in log N_2 density. The dashed line shows the MSIS 2.0 results with the thermospheric relaxation to MSISE-00 turned on (see section 4). (d) Hydrostatic balance metric: pressure gradient (with respect to geopotential height) divided by mass density. When a model is in hydrostatic balance, this quantity equals the reference gravity g_0 (indicated by the black dotted line).

height-resolved temperature and species densities in the 100–200 km region; and (3) a concerted effort to identify and reconcile systematic biases among existing and new temperature and composition data sets, taking into account the strong coupling between temperature and species densities as well as long-term changes in thermospheric climate. The recently launched ICON and GOLD missions partly address the need for new measurements in the 100–200 km region. ICON/MIGHTI (Englert et al., 2017) is measuring temperatures up to ~140 km (Stevens et al., 2018). GOLD is measuring O_2 density profiles from ~130 to 250 km (Eastes et al., 2017). Daedalus (Sarris et al., 2020) is a proposed European Space Agency mission to make in situ height-resolved measurements in the 100–200 km region from an eccentric low-perigee orbit; if selected, this mission could make a strong contribution to middle thermospheric physics and specification in the 2028–2030 timeframe.

6.5. Upper Thermosphere Mass Density

Although MSIS 2.0 does not include a major revision of the thermosphere, it does address some well-documented aspects of upper thermospheric mass density that are not accounted for in MSISE-00. As described in section 4.7, we tuned the O intraannual variation, including solar activity modulation thereof, to orbit-derived mass density. Figure 19 shows bin average residuals as a function of day of year; unlike earlier plots, these residuals are model-minus-data, since in this case we are superposing results from different models and showing individual data sets in separate panels. The MSIS 2.0 densities are ~10% lower overall than MSISE-00, in part because of the ~7% downward revision of the TLE-derived density described in section 3.1 and supported by the ballistic coefficient calculations of Pilinski et al. (2011).

In Figures 19a–19f, the MSIS 2.0 residual means with respect to the TLE density data set are flatter than MSISE-00 across all levels of solar activity not just for the 1986–2005 time interval used to tune the model but also for the independent time period 1971–1985. This indicates that the tuning and the addition of a solar cycle modulation are robust and are consistent with the findings of Emmert and Picone (2010). The MSIS 2.0 residuals are also somewhat flatter with respect to the CHAMP and GOCE data sets (Figures 19g–19k), suggesting that the tuning is also supported by these independent data sets.

At the lower altitude of the GOCE observations (225–300 km), N_2 is a significant contributor to the mass density (~20–60%) and the overall difference between the MSIS 2.0 and MSISE-00 mass density is larger
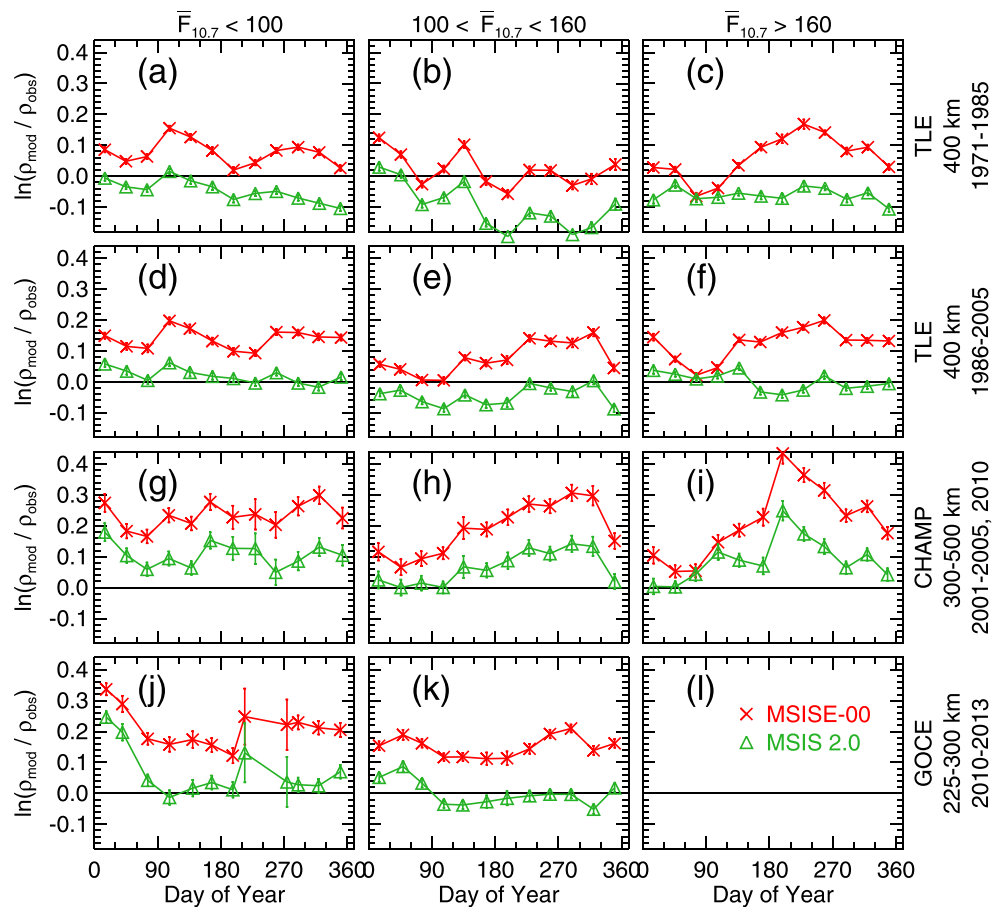
Figure 19. Mean model-minus-data residuals (in natural log space) of MSISE-00 (red x's) and MSIS 2.0 (green triangles) as a function of day of year (30.5 day bins) with respect to the thermospheric mass density data sets indicated to the right of each row: (a–c) orbit-derived (TLE) densities at 400 km altitude from 1971 to 1985, (d–f) TLE densities at 400 km altitude from 1986 to 2005, (g–i) CHAMP accelerometer densities, excluding the anomalous solar minimum years of 2006–2009, (j–l) GOCE accelerometer densities. (left column) Solar minimum conditions, 81 day average $F_{10.7} < 100$, (middle column) solar moderate, $100 < F_{10.7} < 160$, (right column) solar maximum, $F_{10.7} > 160$. Error bars indicate the 1σ estimated uncertainty of the mean.

here (~16%) due to the lower N_2 density in MSIS 2.0 (see section 6.4). Overall, MSIS 2.0 mass densities are ~2% larger than GOCE and ~9% larger than CHAMP (Data Set S7).

Figure S6 is the same as Figure 19 but additionally shows results from the Global Average Mass Density Model (Emmert, 2015a). GAMDM 2.1 is based solely on the 1986–2005 TLE-derived densities and therefore performs better than MSIS with respect to this data set.

Figure 20 illustrates the intraannual variation of MSISE-00 and MSIS 2.0 global average mass density at 400 km, as a function of $F_{10.7}$. The models depict the well-known semiannual oscillation with equinoctial maxima and an annual oscillation with an overall minimum near June solstice. The right-hand panel shows the log ratio of the two models. With the addition of a solar cycle modulation to the O density, at solar maximum MSIS 2.0 has a larger March equinox peak and a deeper June solstice minimum. This is consistent with Bowman et al. (2008) and Emmert and Picone (2010; Figure 5).

7. Summary and Future Development

Like its predecessors, NRLMSIS® 2.0 is an empirical atmospheric model that estimates the average observed behavior of temperature, eight species densities (N_2, O_2, O, He, H, Ar, N, and anomalous O), and mass
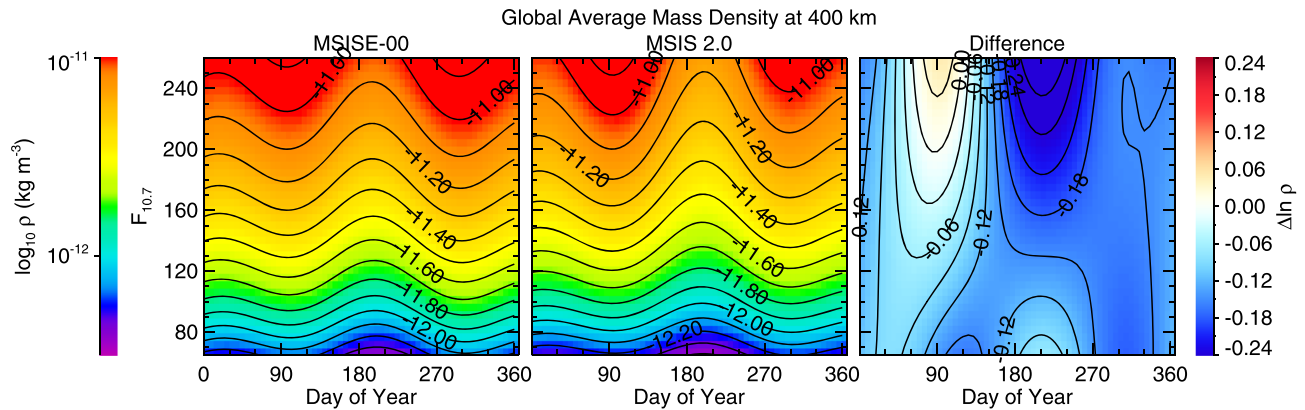
Figure 20. (left) MSISE-00 global average $\log_{10}$ mass density at 400 km, as a function of day of year and $F_{10.7}$. Results are shown for quiet geomagnetic activity conditions ($Ap = 4$). The contour interval is 0.1 (~25%). (middle) Same as left but showing MSIS 2.0. (right) Natural log difference between MSIS 2.0 and MSISE-00, $\ln(\rho_{\text{MSIS 2.0}}/\rho_{\text{MSISE-00}})$. The contour interval is 0.03 (~3%).

density as a parametric function of location, day of year, time of day, solar activity (via the $F_{10.7}$ index), and geomagnetic activity (via the ap index). The model incorporates physical constraints of hydrostatic equilibrium in the well-mixed lower atmosphere (below ~70 km altitude), species-by-species hydrostatic equilibrium (similar to diffusive equilibrium) above ~200 km, and relaxation of thermospheric temperature to an asymptotic exospheric temperature (via the Bates temperature profile). Fortran 90 software to run the model is available in the supporting information and in the repository listed in the acknowledgments.

NRLMSIS 2.0 is a major upgrade to the previous version, NRLMSISE-00 (Picone et al., 2002), with fundamental changes to the formulation and the assimilation of extensive new measurements in the middle and lower atmosphere. The formulation changes include the following:

1. Thermosphere species densities are now fully coupled to the entire temperature profile from the ground to the exosphere, via the introduction of an effective mass profile that approximates the transition from fully mixed to diffusive separation for each species.
2. Geopotential height is now used internally as the vertical coordinate of the model; previous versions used geopotential differences among geometric altitude reference levels.
3. Modeled O density now extends down to 50 km altitude, via the introduction of cubic splines between 50 and 85 km that are decoupled from temperature.
4. Thermal diffusion of He, H, and Ar, which was applied in the thermosphere in previous versions, has been removed.

MSIS 2.0 development focused primarily on altitudes below 100 km. To estimate the parameters of the reformulated model, we assimilated extensive new measurements of temperature in the troposphere, stratosphere, and mesosphere covering the years 2002–2018. The data types used are numerical weather prediction reanalyses, microwave limb sounding, solar occultation, ground-based Na lidars, and infrared passive remote sensing. We also assimilated mesospheric infrared-based measurements of O and H, as well as upper thermospheric mass density derived from satellite orbits.

The temperature data sets in the mesosphere and below are mutually highly consistent, with only a few exceptions that we addressed with appropriate exclusions from the fitting process. The temperature performance of MSIS 2.0 is considerably improved compared to MSISE-00, based on residual analyses of independent samples of the temperature data sets. Biases among MSIS 2.0 and the data sets are typically less than 3 K in the mesosphere and smaller in the stratosphere and troposphere. Residual standard deviations are typically 10–15 K in the upper mesosphere, 6–8 K in the lower mesosphere, and 5–6 K in the stratosphere and troposphere. MSIS 2.0 is warmer overall than MSISE-00 in the upper troposphere and cooler in the stratosphere and mesosphere, which is consistent with the assimilation of

contemporary data sets and first-principles simulations of long-term changes in the atmospheric temperature.

MSIS 2.0 mesospheric O and H density predictions are also improved compared to MSISE-00. In particular, at midlatitudes both species now transition from a winter maximum in the upper thermosphere to a summer maximum in the upper mesosphere, which is consistent with previous data analyses and modeling.

In the fully connected thermosphere and lower atmosphere of MSIS 2.0, the cooler stratospheric and mesospheric temperatures produce N_2 densities in the thermosphere that are ~20% lower than MSISE-00. The software includes an option to recover the MSISE-00 thermospheric N_2 density, but this comes with a large hydrostatic imbalance in the middle thermosphere.

The O density in the MSIS 2.0 upper thermosphere is ~10% lower overall than MSISE-00, mainly as a result of a downward revision of orbit-derived mass density based on theoretical ballistic coefficient modeling. Additionally, the global intraannual variation of thermospheric O now includes a solar activity modulation consistent with previous findings of increased annual and semiannual oscillations at solar maximum.

Besides the changes to N_2 and O, the MSIS 2.0 thermospheric output is largely the same as MSISE-00. Because of difficulties reconciling new thermospheric temperature and density data sets, as well as combining the new data sets with historical mass spectrometer measurements, we have deferred a major thermospheric upgrade of the model. We have concluded that significant advances in climatological specification of the thermosphere require new in situ mass spectrometer measurements of species densities, new techniques for height-resolved temperature and species densities in the 100–200 km region, and a concerted effort to identify and reconcile systematic biases among temperature and composition data sets, taking into account long-term changes in thermospheric climate.

We are currently developing a nitric oxide (NO) component for MSIS, which is slated for inclusion in the next release. Other future plans for the model include the addition of nonmigrating tides, carbon dioxide, and explicit time dependence to account for long-term changes.

Appendix A

A1. Geopotential Height

To calculate the WGS-84 geopotential at locations above the reference ellipsoid, we first convert geodetic latitude and altitude (ϕ_{gd}, h) to Cartesian (x, z) and ellipsoidal (δ, u) coordinates, following the closed-form approach presented by Featherstone and Claessens (2008):

$$
\begin{aligned}
&v = \frac{a}{\sqrt{1 - e^2\sin^2\phi_{gd}}} && \text{Radius of curvature of reference ellipsoid} \\
&x = (v + h)\cos\phi_{gd} && \text{Distance from rotation axis} \\
&z = \left[v\left(1 - e^2\right) + h\right]\sin\phi_{gd} && \text{Distance from equatorial plane} \\
&r^2 = x^2 + z^2 \\
&u^2 = \frac{1}{2}\left(r^2 - E^2\right) + \sqrt{\frac{1}{4}\left(r^2 - E^2\right)^2 + z^2E^2} && \text{Ellipsoidal parameter} \\
&\cos^2\delta = \frac{z^2}{u^2} && \text{Ellipsoidal colatitude} \\
&a = 6378.1370 \text{ km} && \text{Semimajor axis of reference ellipsoid} \\
&e = 0.0818191908426 && \text{Eccentricity of reference ellipsoid} \\
&E = ae && \text{Linear eccentricity}
\end{aligned}
\tag{A1}
$$

We then calculate the geopotential U, including the centrifugal potential $\omega^2 x^2/2$, following Jekeli (2007):
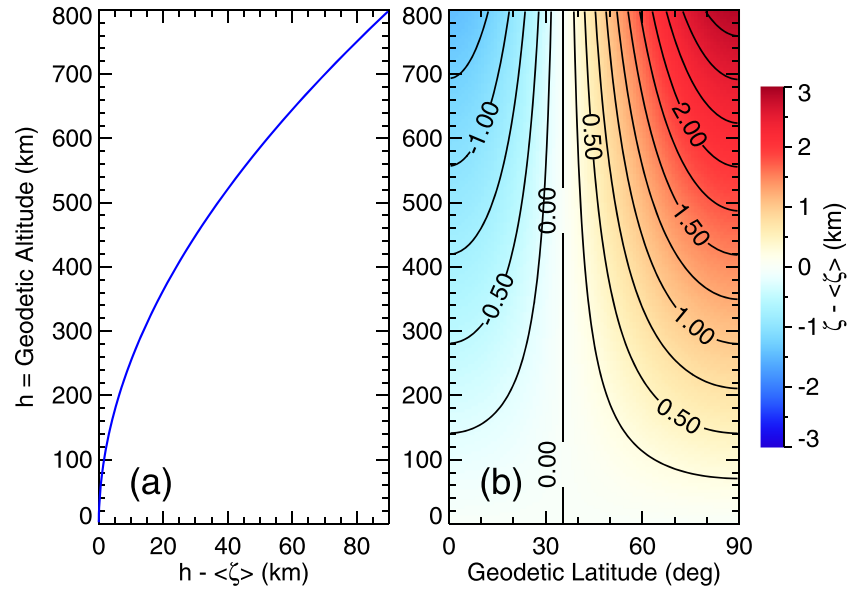
Figure A1. Summary of the conversion of geodetic altitude to geopotential height. (a) The difference between geodetic altitude h and the latitudinally averaged geopotential height $\langle\zeta\rangle$, where $\langle\zeta\rangle = \int_0^\pi \zeta\left(\phi_{gd}, h\right)\cos\phi_{gd}\,d\phi_{gd}$, plotted as a function of h. (b) The difference $\zeta - \langle\zeta\rangle$ between geopotential height and its latitudinally averaged value at a given geodetic altitude, plotted as a function of geodetic altitude and latitude. The contour interval is 0.25 km.

$$U = -\left[\frac{GM}{E}\tan^{-1}\frac{E}{u} + \frac{1}{2}\omega^2 a^2\frac{q}{q_0}\left(\cos^2\delta - \frac{1}{3}\right) + \frac{1}{2}\omega^2 x^2\right]$$

$$q = \frac{1}{2}\left[\left(1 + 3\frac{u^2}{E^2}\right)\tan^{-1}\frac{E}{u} - 3\frac{u}{E}\right]$$

$$q_0 = \frac{1}{2}\left[\left(1 + 3\frac{b^2}{E^2}\right)\tan^{-1}\frac{E}{b} - 3\frac{b}{E}\right] \tag{A2}$$

$$GM = 398600.4418 \text{ km}^3/\text{s}^2 \qquad\qquad \text{Earth's gravitational constant}$$

$$\omega = 7292115.0 \times 10^{-11} \text{ rad/s} \qquad \text{Angular rotation speed}$$

$$b = a\sqrt{1 - e^2} \qquad\qquad\qquad\quad \text{Semiminor axis of reference ellipsoid}$$

Finally, we compute the geopotential height ζ using a reference gravitational acceleration g_0 equal to standard gravity:

$$\zeta = \frac{U - U_0}{g_0}$$

$$U_0 = -62.63685171 \text{ km}^2/\text{s}^2 \quad \text{Potential on the reference ellipsoid} \tag{A3}$$

$$g_0 = 9.80665 \times 10^{-3} \text{ km/s}^2 \quad \text{Standard gravity}$$

Note that for altitudes near the surface, the difference in the numerator of Equation A3 is small compared to the values of U and U_0. Therefore, we carry out the geopotential height calculation in double precision.

Figure A1a shows the difference between geodetic altitude h and latitudinally averaged (area-weighted) geopotential height, as a function of geodetic altitude. The difference increases nonlinearly with altitude; a geodetic altitude of 800 km corresponds to a geopotential height of ~710 km. Figure A1b illustrates the latitude dependence of geopotential height, relative to its latitudinally averaged value at each geodetic altitude. The magnitude of the deviation increases with increasing altitude; at 800 km, the maximum deviation is ~3 km.

The difference between the geopotential height calculated from WGS-84 and the true local geopotential height relative to the geoid is less than ~0.1 km (National Imagery and Mapping Agency, 2000), with the largest differences near the surface. The density scale height of the atmosphere is almost everywhere greater than 5 km, so the simplified geopotential could induce density errors of at most 2%. However, some of that error will be corrected by the spherical harmonic expansion of the pressure and density parameters in the model (section 2.4).

List of Acronyms

ACE	Atmospheric Chemistry Experiment
AIM	Aeronomy of Ice in the Mesosphere (satellite mission)
ALO	Andes Lidar Observatory
ALOMAR	Arctic Lidar Observatory for Middle Atmosphere Research
CFSR	Climate Forecast System Reanalysis
CHAMP	Challenging Minisatellite Payload
Envisat	Environmental Satellite
FTS	Fourier Transform Spectrometer
GOCE	Gravity Field and Steady-State Ocean Circulation Explorer
GOLD	Global-scale Observations of the Limb and Disk (satellite mission)
HALOE	Halogen Occultation Experiment
ICON	Ionospheric Connection Explorer
ISR	Incoherent Scatter Radar
MERRA2	Modern-Era Retrospective analysis for Research and Applications version 2
MIGHTI	Michelson Interferometer for Global High-Resolution Thermospheric Imaging
MIPAS	Michelson Interferometer for Passive Atmospheric Sounding
MLS	Microwave Limb Sounder
MLT	Mesosphere and lower thermosphere
MSIS®	Mass Spectrometer Incoherent Scatter radar
NRL	Naval Research Laborotory
ODRPACK	Orthogonal Distance Regression Package
OSIRIS	Optical Spectrograph and InfraRed Imager System
SABER	Sounding of the Atmosphere using Broadband Emission Radiometry
SCIAMACHY	SCanning Imaging Absorption SpectroMeter for Atmospheric CHartographY
SOFIE	Solar Occultation For Ice Experiment
STAR	Student Training and Atmospheric Research
TIMED	Thermosphere Ionosphere Mesosphere Energetics and Dynamics (satellite mission)
TLE	Two-Line Elements
UARS	Upper Atmosphere Research Satellite
UHF	Ultra high frequency
WACCM-X	Whole Atmosphere Community Climate Model with thermosphere and ionosphere extension
WGS	World Geodetic System
WMO	World Meteorological Organization

Data Availability Statement

NRLMSIS 2.0 Code and all data samples used in this work are available at https://map.nrl.navy.mil/map/pub/nrl/NRLMSIS/NRLMSIS2.0. Raw CFSR Versions 1 and 2 data were obtained from http://nomads.ncdc.noaa.gov/modeldata/cmd_pgbh/ and https://nomads.ncdc.noaa.gov/modeldata/cfsv2_analysis_pgbh/, respectively. MERRA2 data were obtained online (https://goldsmr5.gesdisc.eosdis.nasa.gov/data/MERRA2/M2I3NVASM.5.12.4/). Ground-based lidar and ISR data were obtained from http://www.cedar.openmadrigal.org website. USU Lidar data are also available online (https://doi.org/10.15142/T33H26).

MIPAS data used in this study are available for registered users at http://www.imk-asf.kit.edu/english/308.php website. CHAMP and GOCE accelerometer densities were obtained from http://thermosphere.tudelft.nl website.

References

Arnold, K. S., & She, C. Y. (2003). Metal fluorescence lidar (light detection and ranging) and the middle atmosphere. *Contemporary Physics*, *44*(1), 35–49. https://doi.org/10.1080/00107510302713

Bates, D. R. (1959). Some problems concerning the terrestrial atmosphere above about the 100 km level. *Proceedings of the Royal Society of London, Series A*, *253*, 451–462.

Bermejo-Pantaleón, D., Funke, B., López-Puertas, M., García-Comas, M., Stiller, G. P., von Clarmann, T., et al. (2011). Global observations of thermospheric temperature and nitric oxide from MIPAS spectra at 5.3 μm. *Journal of Geophysical Research*, *116*, A10313. https://doi.org/10.1029/2011JA016752

Bernath, P. F. (2007). The atmospheric chemistry experiment (ACE). *Journal of Quantitative Spectroscopy & Radiative Transfer*, *186*, 3–16. https://doi.org/10.1016/j.jqsrt.2016.04.006

Bowman, B. R., Tobiska, W. K., & Kendra, M. J. (2008). The thermospheric semiannual density response to solar EUV heating. *Journal of Atmospheric and Solar - Terrestrial Physics*, *70*(11–12), 1482–1496. https://doi.org/10.1016/j.jastp.2008.04.020

Bruinsma, S. L. (2015). The DTM-2013 thermosphere model. *Journal of Space Weather and Space Climate*, *5*(A1). https://doi.org/10.1051/swsc/2015001

Chapman, S. (1931). The absorption and dissociative or ionizing effect of monochromatic radiation in an atmosphere on a rotating Earth. *Proceedings of the Physical Society (London)*, *43*(1), 26–45. https://doi.org/10.1088/0959-5309/43/1/305

Chen, H., White, M. A., Krueger, D. A., & She, C. Y. (1996). Daytime mesopause temperature measurements using a sodium-vapor dispersive Faraday filter in lidar receiver. *Optics Letters*, *21*(15), 1093–1095. https://doi.org/10.1364/OL.21.001093

Chu, X., & Papen, G. C. (2005). Resonance fluorescence lidar for measurements of the middle and upper atmosphere. In T. Fujii, & T. Fukuchi (Eds.), *Laser remote sensing* (pp. 179–432). Boca Raton, FL: CRC Press, Taylor & Francis Group. https://doi.org/10.1201/9781420030754.ch5

de Boor, C. (2001). *A Practical Guide to Splines*, *Applied Mathematical Sciences* (27, Rev. ed.). New York, NY: Springer.

Doornbos, E. N., van den IJssel, J., Luehr, H., Foerster, M., & Koppenwallner, G. (2010). Neutral density and crosswind determination from arbitrarily oriented multiaxis accelerometers on satellites. *Journal of Spacecraft and Rockets*, *47*(4), 580–589. https://doi.org/10.2514/1.48114

Drob, D. P., Emmert, J. T., Meriwether, J. W., Makela, J. J., Doornbos, E., Conde, M., et al. (2015). An update to the horizontal wind model (HWM): The quiet time thermosphere. *Earth and Space Science*, *2*, 301–319. https://doi.org/10.1002/2014EA000089

Eastes, R. W., McClintock, W. E., Burns, A. G., Anderson, D. N., Codrescu, M., Correira, J. T., & Oberheide, J. (2017). The global-scale observations of the limb and disk (GOLD) mission. *Space Science Reviews*, *212*(1–2), 383–408. https://doi.org/10.1007/s11214-017-0392-2

Emmert, J. T. (2009). A long-term data set of globally averaged thermospheric total mass density. *Journal of Geophysical Research*, *114*, A06315. https://doi.org/10.1029/2009JA014102

Emmert, J. T. (2015a). Altitude and solar activity dependence of 1967–2005 thermospheric density trends derived from orbital drag. *Journal of Geophysical Research: Space Physics*, *120*, 2940–2950. https://doi.org/10.1002/2015JA021047

Emmert, J. T. (2015b). Thermospheric mass density: A review. *Advances in Space Research*, *56*(5), 773–824. https://doi.org/10.1016/j.asr.2015.05.038

Emmert, J. T., McDonald, S. E., Drob, D. P., Meier, R. R., Lean, J. L., & Picone, J. M. (2014). Attribution of interminima changes in the global thermosphere and ionosphere. *Journal of Geophysical Research: Space Physics*, *119*, 6657–6688. https://doi.org/10.1002/2013JA019484

Emmert, J. T., & Picone, J. M. (2010). Climatology of globally averaged thermospheric mass density. *Journal of Geophysical Research*, *115*, A09326. https://doi.org/10.1029/2010JA015298

Englert, C. R., Harlander, J. M., Brown, C. M., Marr, K. D., Miller, I. J., Stump, J. E., et al. (2017). Michelson interferometer for global high-resolution thermospheric imaging (MIGHTI): Instrument design and calibration. *Space Science Reviews*, *212*(1–2), 553–584. https://doi.org/10.1007/s11214-017-0358-4

Featherstone, W. E., & Claessens, S. J. (2008). Closed-form transformation between geodetic and ellipsoidal coordinates. *Studia Geophysica et Geodaetica*, *52*(1), 1–18. https://doi.org/10.1007/s11200-008-0002-6

Garcia, R. R., Yue, J., & Russell, J. M. (2019). Middle atmosphere temperature trends in the twentieth and twenty-first centuries simulated with the Whole Atmosphere Community Climate Model (WACCM). *Journal of Geophysical Research: Space Physics*, *124*, 7984–7993. https://doi.org/10.1029/2019JA026909

Gelaro, R., McCarty, W., Suárez, M. J., Todling, R., Molod, A., Takacs, L., et al. (2017). The modern-era retrospective analysis for research and applications, version 2 (MERRA–2). *Journal of Climate*, *30*(14), 5419–5454. https://doi.org/10.1175/JCLI-D-16-0758.1

Ginsberg, E. S., & Zaborowski, D. (1975). The dilogarithm function of a real argument. *Communications of the ACM*, *18*(4), 200–202. https://doi.org/10.1145/360715.360722

Gordley, L. L., Hervig, M., Fish, C., Russell, J. M. III, Bailey, S., Cook, J., et al. (2009). The solar occultation for ice experiment (SOFIE). *Journal of Atmospheric and Solar - Terrestrial Physics*, *71*(3–4), 300–315. https://doi.org/10.1016/j.jastp.2008.07.012

Grydeland, T., Lind, F. D., Erickson, P. J., & Holt, J. M. (2005). Software radar signal processing. *Annales Geophysicae*, *23*(1), 109–121.

Harries, J. E., Russell, J. M. III, Tuck, A. F., Gordley, L. L., Purcell, P., Stone, K., et al. (1996). Validation of measurements of water vapor from the Halogen Occultation Experiment (HALOE). *Journal of Geophysical Research*, *101*(D6), 10,205–10,216. https://doi.org/10.1029/95JD02933

Hedin, A. E. (1987). MSIS-86 thermospheric model. *Journal of Geophysical Research*, *92*, 4649–4662. https://doi.org/10.1029/JA092iA05p04649

Hedin, A. E. (1991). Extension of the MSIS thermosphere model into the middle and lower atmosphere. *Journal of Geophysical Research*, *96*, 1159–1172. https://doi.org/10.1029/90JA02125

Hedin, A. E., Reber, C. A., Newton, G. P., Spencer, N. W., Brinton, H. C., Mayr, H. G., & Potter, W. E. (1977). A global thermospheric model based on mass spectrometer and incoherent scatter data MSIS, 2, composition. *Journal of Geophysical Research*, *82*, 2148–2156. https://doi.org/10.1029/JA082i016p02148

Hedin, A. E., Salah, J. E., Evans, J. V., Reber, C. A., Newton, G. P., Spencer, N. W., et al. (1977). A global thermospheric model based on mass spectrometer and incoherent scatter data MSIS, 1, N_2 density and temperature. *Journal of Geophysical Research*, *82*(16), 2139–2147. https://doi.org/10.1029/JA082i016p02139

Hervig, M. E., Gerding, M., Stevens, M. H., Stockwell, R., Bailey, S. M., Russell, J. M., & Stober, G. (2016). Mid-latitude mesospheric clouds and their environment from SOFIE observations. *Journal of Atmospheric and Solar - Terrestrial Physics*, *149*, 1–14. https://doi.org/10.1016/j.jastp.2016.09.004

Höffner, J., & Lübken, F.-J. (2007). Potassium lidar temperatures and densities in the mesopause region at Spitsbergen (78°N). *Journal of Geophysical Research*, *112*, D20114. https://doi.org/10.1029/2007JD008612

Jacchia, L. G. (1971). Revised static models of the thermosphere and exosphere with empirical temperature profiles. SAO special report 332.

Jekeli, C. (2007). Potential theory and static gravity field of the Earth. In T. Herring (Ed.), *Treatise on geophysics* (Vol. 3, pp. 11–42). Amsterdam, Netherlands: Elsevier. https://doi.org/10.1016/B978-044452748-6.00054-7

Jones, M. Jr., Emmert, J. T., Drob, D. P., & Siskind, D. E. (2017). Middle atmosphere dynamical sources of the semiannual oscillation in the thermosphere and ionosphere. *Geophysical Research Letters*, *44*, 12–21. https://doi.org/10.1002/2016GL071741

Jones, M. Jr., Forbes, J. M., & Hagan, M. E. (2014). Tidal-induced net transport effects on the oxygen distribution in the thermosphere. *Geophysical Research Letters*, *41*, 5272–5279. https://doi.org/10.1002/2014GL060698

Kaufmann, M., Zhu, Y., Ern, M., & Riese, M. (2014). Global distribution of atomic oxygen in the mesopause region as derived from SCIAMACHY O(1S) green line measurements. *Geophysical Research Letters*, *41*, 6274–6280. https://doi.org/10.1002/2014GL060574

Keating, G., & Prior, E. (1968). The winter helium bulge. *Space Research*, *8*, 982.

Krueger, D. A., She, C.-Y., & Yuan, T. (2015). Retrieving mesopause temperature and line-of-sight wind from full-diurnal-cycle Na lidar observations. *Applied Optics*, *54*(32), 9469–9489. https://doi.org/10.1364/AO.54.009469

Laštovička, J. (2017). A review of recent progress in trends in the upper atmosphere. *Advances in Space Research*, *163*, 2–13.

Liu, A. Z., Guo, Y., Vargas, F., & Swenson, G. R. (2016). First measurement of horizontal wind and temperature in the lower thermosphere (105–140 km) with a Na Lidar at Andes Lidar Observatory. *Geophysical Research Letters*, *43*, 2374–2380. https://doi.org/10.1002/2016GL068461

Livesey, N. J., Read, W. G., Wagner, P. A., Froidevaux, L., Lambert, A., Manney, G. L., et al. (2017). Aura microwave limb sounder (MLS) version 4.2x level 2 data quality and description document, JPL D-33509 Rev. C.

Lu, X., Chen, C., Huang, W., Smith, J. A., Chu, X., Yuan, T., et al. (2015). A coordinated study of 1-h mesoscale gravity waves propagating from Logan to Boulder with CRRL Na Doppler lidars and temperature mapper. *Journal of Geophysical Research: Atmospheres*, *120*, 10,006–10,021. https://doi.org/10.1002/2015JD023604

Lu, X., Chu, X., Li, H., Chen, C., Smith, J. A., & Vadas, S. L. (2017). Statistical characterization of high-to-medium frequency mesoscale gravity waves by lidar-measured vertical winds and temperatures in the MLT. *Journal of Atmospheric and Solar-Terrestrial Physics*, *162*, 3–15. https://doi.org/10.1016/j.jastp.2016.10.009

Lübken, F.-J. (1999). Thermal structure of the Arctic summer mesosphere. *Journal of Geophysical Research*, *104*, 9135–9149.

March, G. E., Doornbos, N., & Visser, P. N. A. M. (2019). High-fidelity geometry models for improving the consistency of CHAMP, GRACE, GOCE and Swarm Thermospheric Density Data Sets. *Advances in Space Research*, *63*(1), 213–238. https://doi.org/10.1016/j.asr.2018.07.009

Marshall, B. T., Deaver, L. E., Thompson, R. E., Gordley, L. L., McHugh, M. J., Hervig, M. E., & Russell, J. M. III (2011). Retrieval of temperature and pressure using broadband solar occultation: SOFIE approach and results. *Atmospheric Measurement Techniques Discussions*, *3*(6), 5743–5794. https://doi.org/10.5194/amtd-3-5743-2010

McHugh, M., Magill, B., Walker, K. A., Boone, C. D., Bernath, P. F., & Russell, J. M. III (2005). Comparison of atmospheric retrievals from ACE and HALOE. *Geophysical Research Letters*, *32*, L15S10. https://doi.org/10.1029/2005GL022403

McLinden, C. A., Bourassa, A. E., Brohede, S., Cooper, M., Degenstein, D. A., Evans, W. J. F., et al. (2012). OSIRIS: A decade of scattered light. *Bulletin of the American Meteorological Society*, *93*(12), 1845–1863. https://doi.org/10.1175/BAMS-D-11-00135.1

Meier, R. R., Picone, J. M., Drob, D., Bishop, J., Emmert, J. T., Lean, J. L., et al. (2015). Remote sensing of Earth's limb by TIMED/GUVI: Retrieval of thermospheric composition and temperature. *Earth and Space Science*, *2*, 1–37. https://doi.org/10.1002/2014EA000035

Mertens, C. J., Mlynczak, M. G., Lopez-Puertas, M., & Remsberg, E. E. (2002). Impact of non-LTE processes on middle atmospheric water vapor retrievals from simulated measurements of 6.8 μm Earth limb emission. *Geophysical Research Letters*, *29*(9), D1288. https://doi.org/10.1029/2001GL014590

Mlynczak, M. G. (1996). Energetics of the middle atmosphere: Theory and observation requirements. *Advances in Space Research*, *17*(11), 117–126. https://doi.org/10.1016/0273-1177(95)00739-2

Mlynczak, M. G. (1997). Energetics of the mesosphere and lower thermosphere and the SABER experiment. *Advances in Space Research*, *20*(6), 1177–1183. https://doi.org/10.1016/S0273-1177(97)00769-2

Mlynczak, M. G., Hunt, L. A., Marshall, B. T., Mertens, C. J., Marsh, D. R., Smith, A. K., et al. (2014). Atomic hydrogen in the mesopause region derived from SABER: Algorithm theoretical basis, measurement uncertainty, and results. *Journal of Geophysical Research: Atmospheres*, *119*, 3516–3526. https://doi.org/10.1002/2013JD021263

Mlynczak, M. G., Hunt, L. A., Mast, J. C., Thomas Marshall, B., Russell, J. M. III, Smith, A. K., et al. (2013). Atomic oxygen in the mesosphere and lower thermosphere derived from SABER: Algorithm theoretical basis and measurement uncertainty. *Journal of Geophysical Research: Atmospheres*, *118*, 5724–5735. https://doi.org/10.1002/jgrd.50401

Mlynczak, M. G., Hunt, L. A., Russell, J. M. III, & Marshall, B. T. (2018). Updated SABER night atomic oxygen and implications for SABER ozone and atomic hydrogen. *Geophysical Research Letters*, *45*, 5735–5741. https://doi.org/10.1029/2018GL077377

Mlynczak, M. G., Hunt, L. H., Mertens, C. J., Marshall, B. T., Russell, J. M. III, López Puertas, M., et al. (2013). Radiative and energetic constraints on the global annual mean atomic oxygen concentration in the mesopause region. *Journal of Geophysical Research: Atmospheres*, *118*, 5796–5802. https://doi.org/10.1002/jgrd.50400

Mlynczak, M. G., & Solomon, S. (1993). A detailed evaluation of the heating efficiency in the middle atmosphere. *Journal of Geophysical Research*, *98*(D6), 10,517–10,541. https://doi.org/10.1029/93JD00315

National imagery and mapping agency (2000). Department of defense world geodetic system 1984 (NIMA Technical Report TR8350.2). Retrieved from http://earth-info.nga.mil/GandG/publications/tr8350.2/wgs84fin.pdf

Oberheide, J., Forbes, J. M., Zhang, X., & Bruinsma, S. L. (2011). Climatology of upward propagating diurnal and semidiurnal tides in the thermosphere. *Journal of Geophysical Research*, *116*, A11306. https://doi.org/10.1029/2011JA016784

Panka, P. A., Kutepov, A. A., Rezac, L., Kalogerakis, K. S., Feofilov, A. G., Marsh, D., et al. (2018). Atomic oxygen retrieved from the SABER 2.0- and 1.6-μm radiances using new first-principles nighttime OH(v) model. *Geophysical Research Letters*, *45*, 5798–5803. https://doi.org/10.1029/2018GL077677

Picard, A., Davis, R. S., Gläser, M., & Fujii, K. (2008). Revised formula for the density of moist air (CIPM–2007). *Metrologia*, *45*(2), 149–155. https://doi.org/10.1088/0026-1394/45/2/004

Picone, J. M., Emmert, J. T., & Drob, D. P. (2016). Consistent static models of local thermospheric composition profiles. arXiv:1607.03370v1 [physics.space-ph]

Picone, J. M., Hedin, A. E., Drob, D. P., & Aikin, A. C. (2002). NRLMSISE-00 empirical model of the atmosphere: Statistical comparisons and scientific issues. *Journal of Geophysical Research*, *107*(A12), 1468. https://doi.org/10.1029/2002JA009430

Picone, J. M., Meier, R. R., & Emmert, J. T. (2013). Theoretical tools for studies of low-frequency thermospheric variability. *Journal of Geophysical Research: Space Physics*, *118*, 5853–5873. https://doi.org/10.1002/jgra.50472

Pilinski, M. D., Argrow, B. M., & Palo, S. E. (2011). Drag coefficients of satellites with concave geometries: Comparing models and observations. *Journal of Spacecraft and Rockets*, *48*(2), 312–325. https://doi.org/10.2514/1.50915

Qian, L., Burns, A. G., Solomon, S. S., Smith, A. K., McInerney, J. M., Hunt, L. A., et al. (2018). Temporal variability of atomic hydrogen from the mesopause to the upper thermosphere. *Journal of Geophysical Research: Space Physics*, *123*, 1006–1017. https://doi.org/10.1002/2017JA024998

Qian, L., Solomon, S. C., & Kane, T. J. (2009). Seasonal variation of thermospheric density and composition. *Journal of Geophysical Research*, *114*, A01312. https://doi.org/10.1029/2008JA013643

Randel, W. J., Smith, A. K., Wu, F., Zou, C. Z., & Qian, H. (2016). Stratospheric temperature trends over 1979–2015 derived from combined SSU, MLS, and SABER satellite observations. *Journal of Climate*, *29*(13), 4843–4859. https://doi.org/10.1175/JCLI-D-15-0629.1

Reber, C. A., & Hays, P. B. (1973). Thermospheric wind effects on the distribution of helium and argon in the Earth's upper atmosphere. *Journal of Geophysical Research*, *78*(16), 2977–2991. https://doi.org/10.1029/JA078i016p02977

Russell, J. M. III, Bailey, S. M., Gordley, L. L., Rusch, D. W., Horányi, M., Hervig, M. E., et al. (2009). Aeronomy of Ice in the Mesosphere (AIM): Overview and early science results. *Journal of Atmospheric and Solar - Terrestrial Physics*, *71*(3–4), 289–299. https://doi.org/10.1016/j.jastp.2008.08.011

Russell, J. M. III, Gordley, L. L., Park, J. H., Drayson, S. R., Hesketh, W. D., Cicerone, R. J., et al. (1993). The halogen occultation experiment. *Journal of Geophysical Research*, *98*(D6), 10,777–10,797. https://doi.org/10.1029/93JD00799

Russell, J. M. III, Mlynczak, M. G., Gordley, L. L., Tansock, J. J. Jr., & Esplin, R. W. (1999). Overview of the SABER experiment and preliminary calibration results. *Proceedings of SPIE*, *3756*, 277. https://doi.org/10.1117/12.366382

Saha, S., Moorthi, S., Pan, H. L., Wu, X., Wang, J., Nadiga, S., et al. (2010). The NCEP climate forecast system reanalysis. *Bulletin of the American Meteorological Society*, *91*(8), 1015–1058. https://doi.org/10.1175/2010BAMS3001.1

Saha, S., Moorthi, S., Wu, X., Wang, J., Nadiga, S., Tripp, P., et al. (2014). The NCEP climate forecast system version 2. *Journal of Climate*, *27*(6), 2185–2208. https://doi.org/10.1175/JCLI-D-12-00823.1

Salah, J., & Evans, J. (1973). Measurements of thermospheric temperatures by incoherent scatter radar. *Space Research*, *13*, 267–286.

Sarris, T. E., Talaat, E. R., Palmroth, M., Dandouras, I., Armandillo, E., Kervalishvili, G., et al. (2020). Daedalus: A low-flying spacecraft for in situ exploration of the lower thermosphere-ionosphere. *Geoscientific Instrumentation, Methods and Data Systems*, *9*(1), 153–191. https://doi.org/10.5194/gi-9-153-2020

Schwartz, M. J., Lambert, A., Manney, G. L., Read, W. G., Livesey, N. J., Froidevaux, L., et al. (2008). Validation of the Aura Microwave Limb Sounder temperature and geopotential height measurements. *Journal of Geophysical Research*, *113*, D15S11. https://doi.org/10.1029/2007JD008783

She, C. Y., Vance, J. D., Williams, B. P., Krueger, D. A., Moosmuller, H., Gibson-Wilde, D., & Fritts, D. C. (2002). Lidar studies of atmospheric dynamics near polar mesopause. *Eos*, *83*(27), 289–293. https://doi.org/10.1029/2002EO000206

Sheese, P. E., Llewellyn, E. J., Gattinger, R. L., Bourassa, A. E., Degenstein, D. A., Lloyd, N. D., & McDade, I. C. (2010). Temperatures in the upper mesosphere and lower thermosphere from OSIRIS observations of O_2 A-band emission spectra. *Canadian Journal of Physics*, *88*, 919–925. https://doi.org/10.1139/P10-093

Sheese, P. E., McDade, I. C., Gattinger, R. L., & Llewellyn, E. J. (2011). Atomic oxygen densities retrieved from optical spectrograph and infrared imaging system observations of O_2 A-band airglow emission in the mesosphere and lower thermosphere. *Journal of Geophysical Research*, *116*, D01303. https://doi.org/10.1029/2010JD014640

Siskind, D. E., Merkel, A. W., Marsh, D. R., Randall, C. E., Hervig, M. E., Mlynczak, M. G., & Russell, J. M. III (2018). Understanding the effects of polar mesospheric clouds on the environment of the upper mesosphere and lower thermosphere. *Journal of Geophysical Research: Atmospheres*, *123*, 11,705–11,719. https://doi.org/10.1029/2018JD028830

Siskind, D. E., Mlynczak, M. G., Marshall, T., Friedrich, M., & Gumbel, J. (2015). Implications of odd oxygen observations by the TIMED/SABER instrument for lower D region ionospheric modeling. *Journal of Atmospheric and Solar - Terrestrial Physics*, *124*, 63–70. https://doi.org/10.1016/j.jastp.2015.01.014

Smith, A. K., Marsh, D. R., Mlynczak, M. G., & Mast, J. C. (2010). Temporal variations of atomic oxygen in the upper mesosphere from SABER. *Journal of Geophysical Research*, *115*, D18309. https://doi.org/10.1029/2009JD013434

Smith, J. A., & Chu, X. (2015). High-efficiency receiver architecture for resonance-fluorescence and Doppler lidars. *Applied Optics*, *54*(11), 3173–3184. https://doi.org/10.1364/AO.54.003173

Solomon, S. C., Liu, H.-L., Marsh, D. R., McInerney, J. M., Qian, L., & Vitt, F. M. (2018). Whole atmosphere simulation of anthropogenic climate change. *Geophysical Research Letters*, *45*, 1567–1576. https://doi.org/10.1002/2017GL076950

Stevens, M. H., Deaver, L. E., Hervig, M. E., Russell, J. M. III, Siskind, D. E., Sheese, P. E., et al. (2012). Validation of upper mesospheric and lower thermospheric temperatures measured by the solar occultation for ice experiment. *Journal of Geophysical Research*, *117*, D16304. https://doi.org/10.1029/2012JD017689

Stevens, M. H., Englert, C. R., Harlander, J. M., England, S. L., Marr, K. D., Brown, C. M., & Immel, T. J. (2018). Retrieval of lower thermospheric temperatures from O_2 A band emission: The MIGHTI experiment on ICON. *Space Science Reviews*, *214*, 4. https://doi.org/10.1007/s11214-017-0434-9

Sutton, E. K. (2016). Interhemispheric transport of light neutral species in the thermosphere. *Geophysical Research Letters*, *43*, 12,325–12,332. https://doi.org/10.1002/2016GL071679

Swenson, G. R., Salinas, C. C. J. H., Vargas, F., Zhu, Y., Kaufmann, M., Jones, M. Jr., et al. (2019). Determination of global mean eddy diffusive transport in the mesosphere and lower thermosphere from atomic oxygen and carbon dioxide climatologies. *Journal of Geophysical Research: Atmospheres*, *124*, 13,519–13,533. https://doi.org/10.1029/2019JD031329

Tapping, K. F. (2013). The 10.7 cm solar radio flux (F10.7). *Space Weather*, *11*, 394–406. https://doi.org/10.1002/swe.20064

Waters, J. W., Froidevaux, L., Harwood, R. S., Jarnot, R. F., Pickett, H. M., Read, W. G., et al. (2006). The earth observing system microwave limb sounder (EOS MLS) on the Aura satellite. *IEEE Transactions on Geoscience and Remote Sensing*, *44*(5), 1075–1092. https://doi.org/10.1109/TGRS.2006.873771

Weimer, D. R., Mlynczak, M. G., Emmert, J. T., Doornbos, E., Sutton, E. K., & Hunt, L. A. (2018). Correlations between the thermosphere's semiannual density variations and infrared emissions measured with the SABER instrument. *Journal of Geophysical Research: Space Physics*, *123*, 8850–8864. https://doi.org/10.1029/2018JA025668

WMO (2014). Guide to Meteorological Instruments and Methods of Observation (WMO-No. 8). Geneva, Switzerland: World Meteorological Organization (WMO). Retrieved from https://www.wmo.int/pages/prog/www/IMOP/CIMO-Guide.html

Zhang, S.-R., Holt, J. M., & Kurdzo, J. (2011). Millstone Hill ISR observations of upper atmospheric long-term changes: Height dependency. *Journal of Geophysical Research*, *116*, A00H05. https://doi.org/10.1029/2010JA016414

Zhang, S. R., & Holt, J. M. (2013). Long-term ionospheric cooling: Dependency on local time, season, solar activity, and geomagnetic activity. *Journal of Geophysical Research: Space Physics*, *118*, 3719–3730. https://doi.org/10.1002/jgra.50306

Zhu, Y., & Kaufmann, M. (2019). Consistent nighttime atomic oxygen concentrations from O_2 A-band, O(1S) green line, and OH airglow measurements as performed by SCIAMACHY. *Geophysical Research Letters*, *46*, 8536–8545. https://doi.org/10.1029/2019GL083550

Zwolak, J. W., Boggs, P. T., & Watson, L. T. (2007). Algorithm 869: ODRPACK95, 2007: A weighted orthogonal distance regression code with bound constraints. *Association for Computing Machinery*, *33*. https://doi.org/10.1145/1268776.1268782